Plate tectonics drive deep biosphere microbial community composition

Katherine M. Fullerton[1], Matthew Schrenk[2], Mustafa Yücel[3], Elena Manini[4], Daniele Fattorini[5,6], Marta di Carlo[5,6], Francesco Regoli[5,6], Mayuko Nakagawa[7], Francesco Smedile[4,9], Costantino Vetriani[8,9], Heather Miller[2], Shaunna M. Morrison[10], Maria Martinez[11], J. Maarten de Moor[11,12], Peter H. Barry[13], Donato Giovannelli[4,7,9,14*], and Karen G. Lloyd[1*]

[1]University of Tennessee, Knoxville, TN, USA
[2]Michigan State University, East Lansing, MI, USA
[3]Institute of Marine Sciences, Middle East Technical University, Erdemli, Turkey.
[4]Institute for Marine Biological and Biotechnological Resources, National Research Council of Italy (CNR-IRBIM), Ancona, Italy
[5]Dipartimento di Scienze della Vita e dell'Ambiente (DISVA), Università Politecnica delle Marche (UNIVPM), Ancona, Italy.
[6]CoNISMa, Consorzio Nazionale Interuniversitario Scienze del Mare, Rome, Italy
[7]Earth-Life Science Institute, Tokyo Institute for Technology, Tokyo, Japan.
[8]Departmnet od Biochemistry and Microbiology, Rutgers University, New Brunswick, USA
[9]Department of Marine and Coastal Science, Rutgers University, New Brunswick, NJ, USA
[10]Carnegie Institution for Science, Washington, DC
[11]Observatorio Volcanológico y Sismológico de Costa Rica (OVSICORI), Universidad Nacional, Heredia, Costa Rica.
[12]Department of Earth and Planetary Sciences, University of New Mexico, Albuquerque, NM, USA
[13]Woods Hole Oceanographic Institution, Woods Hole, MA, USA
[14]Department of Biology, University of Naples Federico II, Naples, Italy

*Corresponding authors: donato.giovannelli@unina.it and klloyd@utk.edu

Abstract

Deep subsurface microbes comprise one of the largest biospheres on Earth, altering the volatiles that move between the deep Earth and the surface. One of the most compelling - yet elusive - questions in geomicrobiology is how large-scale tectonic processes, such as plate subduction at convergent margins, affect the distribution and function of subsurface microorganisms. Here we show that the microbial distribution across a transect of a subducting convergent margin is explained by differences in subducting parameters between the East Pacific Rise (EPR) in north Costa Rica and the Cocos-Nazca Spreading (CNS) Center in central Costa Rica. The differences in slab dip angle and extensional versus compressional stress regime in the volcanic arc affect microbial distributions through the changes these deep structures exert on fluid geochemistry. In turn, these microbial communities affect the geochemistry and mineralogy of the system by catalyzing iron and sulfur redox reactions and fixing CO_2 into biomass. We conclude that the microbial community structure tracks tectonic processes across this subduction zone and participates in deep volatile cycling and carbon sequestration.

Introduction

The deep subsurface biosphere is one of the largest biomes on Earth and it drives a wide range of key biogeochemical transformations (*1*). At individual sites, the composition of microbial communities has been linked to geochemical parameters such as temperature, pH, metal concentrations, and energy availability (*2*–*4*). However, it is unknown whether subsurface biology is connected to the geological setting across larger (>100km) tectonic provinces. Here, we assayed microbial community compositions in surface expressions of deeply-sourced hydrothermal fluids across a convergent margin transect. We determined whether the microbes were connected to underlying tectonic processes through the impacts that these processes have on geochemistry.

Convergent margins are important conduits connecting the vast store of carbon in the deep Earth with the surface. As denser oceanic plates subduct beneath continental crust, carbon compounds and other volatile material are transferred from Earth's surface to its interior (*5*). These substances are also recycled back to the surface at these plate boundaries (*5*) - making them some of the most dynamic regions on the planet. Here, fluid release, magmatism, and deformation provide diverse habitats that may be colonized by deep life, since temperature, pH, redox, elemental compositions, pressure, and salinity vary widely across plate margins (*6*). While the depth to the subducting slab can be hundreds of kilometers, the deep biosphere is thought to be limited to the upper few kilometers where temperatures are below ~120°C (*7*). Even though they are separated by many kilometers, the upward mobility of deeply-sourced fluids may connect subsurface microbes to the deep geological structures below them. Variations in microbial community compositions of New Zealand convergent margin hot springs have been linked to dispersal and local surficial geochemistry (*8*), but no large-scale survey has investigated potential interdependence between microbiology and plate tectonics across a plate boundary.

To explore the large-scale connection between subsurface microbiology and geochemical processes, we compared bacterial community composition, aqueous and solid phase geochemistry, and volatile emissions across the Costa Rican convergent margin (Fig. 1). Here, the Cocos oceanic plate subducts beneath the Caribbean plate at a rate of 70-90mm/yr (*9*), forming the Middle America Trench. The shallow subduction geometry promotes slab dehydration prior to reaching the magma generation zone, allowing for the release of large fluxes of organic carbon and reduced chemical species into the overlying plate in the outer forearc, forearc, and arc (*10*, *11*). Much of the CO_2 from the slab beneath the forearc is sequestered as subsurface calcite and microbial biomass, trapping carbon that would otherwise be delivered to the mantle (*12*). Remarkably, the continental extension of the oceanic plate boundary between the East Pacific Rise (EPR) and Cocos Nazca Spreading center (CNS) is identifiable by a shift in the carbon isotopic composition of arc and forearc fluid and gas emissions (*12*), suggesting tight coupling between deep tectonic structure and surface-expressing fluids.

Within the Central American Volcanic Arc (CAVA), only two hot spring systems have been characterized microbiologically. Alkaline geothermal springs in the Santa Elena ophiolite, the northernmost geotectonic complex in the Costa Rica forearc, support low cell densities (2.0×10^4-1.51×10^5 cells/mL) of microorganisms involved in hydrogen oxidation and methane cycling (*13*). Strains of *Thiobacillus* spp. were cultured from the acid crater lake of Poás Volcano in central Costa Rica (*14*) and a 16S rRNA gene amplicon study identified a single operational taxonomic unit (OTU) of *Acidiphilium* spp. there (*15*). In 2017, we collected two types of samples from 21 hot springs across northern and central Costa Rica: 1) fresh fluids actively venting from the subsurface, and 2) sediments accumulated in surface pools at the vent source of those hot spring fluids. The sites ranged from heavily influenced by human activities (spas/resorts and cattle ranches) to jungles with low perturbation. The sites covered the full range of subduction provinces from the outer forearc, characterized by upper plate mafic rock and a shallow slab depth (20-40 km), to the forearc and arc (50-100 km slab depth), including volcanoes from the northern Guanacaste Geothermal Province, as well as Arenal, Poás, and Irazú stratovolcanoes in the Central Cordillera (Fig. 1).

Cell abundances ranged from 1.5×10^3 to 3.3×10^6 cells/mL, typical of other hydrothermal systems (*2*, *4*), and were not significantly different between the outer forearc vs. forearc/arc or between the sites overlying the EPR vs. CNS plates (n=23, p>0.01, Wilcoxon test, Fig. S1). Eleven sites produced high-quality bacterial 16S rRNA gene libraries in both fluids and sediments and seven more sites were successful only for fluids or sediments, altogether comprising 56,142 total amplicon sequence variants (ASVs).

The dissolved organic carbon (DOC) in these hot spring fluids originated almost entirely through chemosynthesis, since the $\delta^{13}C$ values correlated closely with $\delta^{13}C$ values of dissolved inorganic carbon (DIC), and the DIC was derived from an admixture between slab and mantle-derived fluids. This suggests very little input from surface-derived organic matter, which demonstrated $\delta^{13}C$ values consistent with a photosynthetic origin and no variation across the convergent margin (*12*). Photosynthetic biomarkers were found in low abundances, with <5 µg/g total photosynthetic pigments in the surface sediments and <1% and <4% chloroplast-related 16S rRNA genes in deep fluids and surface sediments, respectively. Further, the bacterial community membership in fluids and sediments were similar within each site (Adonis, unweighted UniFrac $r^2 = 0.036$, $p = 0.26$, Table S1). Overall, these findings suggest that chemosynthetic fixation of mantle/slab derived CO_2 drives microbial processes in fluids and imply a deep-fluid origin of sediment microbes.

Bacterial community composition varied significantly with the geologic province across the subduction zone (outer forearc, forearc, and arc), across the boundary between the EPR and CNS tectonic plates, and with the dominant bedrock types (Table S2, Fig. S2; Adonis, weighted Jaccard, $p < 0.01$). As expected from other studies of microbial diversity in hydrothermal fluids (*e.g.,* (*3*)), temperature and pH negatively correlated with each other and these two geochemical parameters correlated with bacterial community composition (Figs. 2a, S2, S3, S4, Jaccard similarity Table S3, S4). Phyla with thermophilic isolates such as *Hydrothermae*, *Thermatogae*, *Aquificae*, as well as phyla from the Candidatus 'Atribacteria' and unclassified bacteria increased in relative 16S rRNA gene abundances with temperature and decreased with pH, with the opposite trend for *Proteobacteria*, a few uncultured phyla, *Cloacimonetes*, and others (Fig. S4). Most phyla, however, did not vary much with temperature and pH (Fig. S4), suggesting that the distribution of bacterial communities across this convergent margin was not a simple function of these two parameters.

A ternary plot of aqueous anions (Cl^-, SO_4^{2-}, and DIC) (*16*) was found to distinguish between: a) acidic (pH 0 to 3) chloride-sulfate waters associated with direct absorption of magmatic gases at arc sites (red and burgundy symbols), b) relatively sulfate-poor peripheral geothermal waters intermediate in composition between deeply-derived chloride-rich waters and soda springs characteristic of flank volcanic sites and forearc locations (orange symbols), and c) alkaline outer forearc sites that are relatively poor in both sulfate and chloride (blue symbols). Quepos hot springs (QH), a forearc site, falls at anomalously high Cl^- content with pH of 8.7, suggesting relatively well-equilibrated deep fluids (*16*) (purple, Fig. 2b). These deep structure-driven geochemical differences correlated well with bacterial community composition (Fig. 2c).

Further fluid composition distinctions were evident in cation relationships (Fig. 2d; Mg^{2+}, Ca^{2+}, and Na^{+}+K^{+}). Acidic arc volcanic sites (yellow symbols) were relatively enriched in Ca^{2+} as these fluids are typically saturated with respect to gypsum *(e.g.* (*17*)*).* Flank geothermal sites and forearc springs (purple symbols) defined a trend away from the Ca^{2+} apex, likely due to fluid neutralization accompanied by precipitation of calcite. Indeed, large travertine mounds were observed at many of these sites. The outer forearc as well as some forearc sites fell near the $Na^+ + K^+$ apex, suggesting that these were mature deep fluids with good equilibration between feldspars and clays (*16*). These geochemical provinces also tightly correlated with bacterial community composition (Fig. 2e; Table S2), with the exception of Poás Lake (PL), which, as a hyper-acid active volcanic crater lake, was unique from all other sites. Thus, tectonic province (arc, forearc, outer forearc), fluid composition, and bacterial community composition are all intricately linked and ultimately tied to both primary subduction zone processes and secondary processes associated with the position relative to the trench and depth to the slab.

Multiple lines of evidence suggest that the correlations previously described are driven by a direct influence of a deeply-sourced geochemistry on microbial communities. Genera of known iron-oxidizers (like *Gallionella*, *Geobacter* and *Ferritrophicum*, among others, Fig. 3a) are present almost exclusively in the central arc sites. On the other hand, sequences related to known sulfide-oxidizers (like *Sulfurihydrogenibium*) are mainly present in the northern forearc/arc sites (Fig. 3b). In the central region, the only *Sulfurihydrogenibium*-related species were from the volcanic crater lake site, PL. Differences in the structural geology and volcanology of the two provinces could account for these differences in microbial distribution. The large calderas associated with extensional tectonics and a steeper subduction slab in northern Costa Rica Guanacaste Geothermal Provice (Figure 1a) host well-developed geothermal systems (*18*), which often contain abundant sulfide due to volcanic volatile input. We hypothesize that this reduced sulfur, besides supporting sulfide- and thiosulfate-oxidizing bacteria, is also responsible for the lack of free iron (II) available for iron-oxidizers. Sulfide reacts with iron (II) to form iron-sulfide and pyrite (*19*), and can be a powerful scavenger limiting iron availability for respiration. In contrast, the stratovolcanoes of the Central Cordillera sites have higher gas emission temperatures dominated by SO_2, and smaller, comparatively less mature hydrothermal systems. In these sites, sulfide was present only near the main volcanic conduit with a high input from deep magmatic waters (like in PL (*20*)). The surrounding hot springs are thus enriched in iron leached from water-rock interactions at depth, making iron (II) available for microbial oxidation. Our Scanning Electron Microscopy and Energy-dispersive X-ray spectroscopy (SEM-EDS) analysis coupled with X-ray Diffraction (XRD) analysis of the hot-spring sediments support this hypothesis. Twisted stalks of iron hydroxide, hallmarks of microbial mediated iron-oxidation (*21*), were present in the Central Cordillera stratovolcano sites (Figs. 3c, S6, S7), while pyrite framboids were identified in the hot-spring sediments of northern sites (Fig. 3d, S5a-d). Orange iron-rich precipitations abundant enough to coat most of the rocks in the area were found only at the southern arc sites TC, ST, QN, CY and RV (Figs. 3e, 3f, S6, S7). The structural differences between the volcanology of the two areas are ultimately connected with differences in the properties of the subducting slab between the northern EPR and the central CNS, primarily the dip angle and extensional versus compressional local stress regime in the volcanic arc (*22*, *23*). Sequences similar to known sulfate-reducing (*Sulfuritalea* and *Desulfotomaculum)* and sulfide-oxidizing (*Thiothrix* and *Geothrix*) bacteria were only found in the outer forearc/forearc sites and typically linked to more immature waters with sulfide supplied by biological organic matter decay and sulfate-reduction (Fig. 2c).

Most of the genera listed above contain cultured chemolithoautotrophs (*24–28*). Calcite deposition is often catalyzed by chemolithoautotrophic microbes, which increase alkalinity through CO_2 consumption and also nucleate the precipitation of minerals (*29*). Therefore, these genera may be responsible for the biological CO_2-sink identified for the Costa Rica convergent margin (*12*), and serve as the primary producers for the subsurface microbial ecosystem in this region. However, the catabolic reactions fueling this chemolithoautotrophy vary across the arc structure, with catabolism of sulfate and sulfide in the outer forearc, sulfur in the forearc/arc, and iron only in the central forearc/arc. These variations provide a possible explanation for the different fractionation factors between $\delta^{13}C$ values of DOC and DIC in central (5.8‰ ± 2.2‰) vs. the northern (10.9‰ ± 1.6‰) zones (*12*). Collectively, these results provide strong evidence that deep geological structures dictate the composition of the bacterial community of surface-expressing fluids at the scale of an entire subducting plate. In turn, these biological communities affect the geochemistry and mineralogy by catalyzing iron and sulfur redox reactions and fixing CO_2.

To determine which environmental variables best explain the distribution of subsurface bacteria across the convergent margin, we used a co-occurrence network approach coupled to Random Forest variable ranking (Fig. 4). Most cliques of co-occuring ASVs were taxonomically diverse (Fig. S8), suggesting that ecosystem function rather than taxonomic similarity drove microbial distribution. Clique 4 (Table S5) correlated positively with DOC concentrations (Fig. 4b) and contained the main chemolithoautotrophs that may be driving DOC production across the convergent margin transect. Clique 4 was dominated by *Sulfurihydrogenibium* spp. (55%) which, along with *Hydrogenophilus* spp. (>10%), are facultative autotrophic sulfur and hydrogen oxidizers (*30*). Cliques 1 and 3 correlated more loosely with these chemolithoautotrophs and included known heterotrophic genera, suggesting that these organisms were dependent on primary production from the members of clique 4. Members of clique 3 correlated most closely with iron, suggesting its importance either as a metal cofactor or as a respiratory substrate for them (Fig. 4b).

Clique 2 correlated with pH and clique 9 correlated inversely with DIC (Fig. 4b). Clique 9 was dominated by *Thiothrix* spp. (65%) with lesser proportions of *Hydrogenophilaceae* (which was the most abundant organism in clique 2 at 12%) and *Sulfuritalea*, all of whose cultured members are chemolithoautotrophic sulfur oxidizers. The low DIC and high pH sites in which these organisms were found in the highest relative abundances were the outer forearc sites, where the greatest extent of calcite sequestration was observed (*12*). Therefore, these clades might have adaptations, such as high affinity for DIC, that allow them to sequester carbon even though the high pH, low DIC, and low DOC suggest that they are DIC-limited (*12*). Clique 6 was dominated by *Aquabacterium* spp. (46%) and *Alishewanella* spp. (22%), both of which are common heat-tolerant bacteria from soils (*31*) and freshwater (*32*). Clique 6, therefore, served as an internal negative control, showing that when surface-associated bacteria were washed into the system, they did not correlate with deep subsurface geological parameters.

Overall, our data suggest that the deep subsurface microbial community of a ~400 km subduction segment in Costa Rica cohesively responds to geochemical signals that can ultimately be traced to deep tectonic processes. This would imply that microbial community compositions are predictable on the planetary-scale based on the tectonic setting. Microbial communities, in turn, drive the large-scale deposition of calcite (*12*) and other minerals, influencing globally important element cycling and mineral precipitation and dissolution. Collectively, our work shows that volatiles and elements mobilized from the descending slab can be significantly altered by interaction with the deep subsurface biosphere on their trek back to the surface, resulting in a previously unrecognized coupling between geological and biological feedbacks in a convergent margin.

Acknowledgments

This work was principally supported by a grant from the Alfred P. Sloan Foundation and the Deep Carbon Observatory to P.H.B., J.M.dM, D.G, and K.G.L, with DNA sequencing support from the Census of Deep Life. In addition, K.G.L. was supported by NSF OCE-1431598, NASA Exobiology NNX16AL59G, and Simons Foundation 404586. P.H.B. was supported by NSF grant 1144559 during a portion of this project. D.G. was supported by an NSF grant (MCB 15–17567) and an ELSI Origins Network (EON) research Fellowship, which is supported by a grant from the John Templeton Foundation. D.G. was also partially supported a Deep Life Modeling and Visualization Fellowship, which is supported by the Deep Carbon Observatory. D.G. acknowledges the support of the project ENIGMA (NASA Astrobiology Institute cycle 8) Grant Number 80NSSC18M0093. The opinions expressed in this publication are those of the authors and do not necessarily reflect the views of the John Templeton Foundation. This work was further supported in part by JSPS KAKENHI grants (JP17K14412, JP17H06105, JP17H02989) awarded to M.N. M.Y. was supported by a DEKOSIM grant (BAP-08-11-DPT.2012K120880), financed by the Strategy and Budget Ministry of Turkey. We thank Patricia Barcala Dominguez for assistance with figure illustration.

References

1. C. Magnabosco et al., The biomass and biodiversity of the continental subsurface. Nat. Geosci. 11, 707–717 (2018).

2. J. P. Amend, A. Teske, Expanding frontiers in deep subsurface microbiology. *Palaeogeogr. Palaeoclimatol. Palaeoecol.* **219**, 131–155 (2005).

3. D. R. Colman *et al.*, Geobiological feedbacks and the evolution of thermoacidophiles. *ISME J.* **12**, 225–236 (2018).

4. J. Reveillaud *et al.*, Subseafloor microbial communities in hydrogen-rich vent fluids from hydrothermal systems along the Mid-Cayman Rise. *Environ. Microbiol.* **18**, 1970–1987 (2016).

5. P. B. Kelemen, C. E. Manning, Reevaluating carbon fluxes in subduction zones, what goes down, mostly comes up. *Proc. Natl. Acad. Sci.* **112**, E3997–E4006 (2015).

6. N. Merino *et al.*, Living at the extremes: Extremophiles and the limits of life in a planetary context. *Front. Microbiol.* **10** (2019).

7. O. Plümper *et al.*, Subduction zone forearc serpentinites as incubators for deep microbial life. *Proc. Natl. Acad. Sci. USA*. **114**, 4324–4329 (2017).

8. C. P. Kempes *et al.*, Drivers of bacterial maintenance and minimal energy requirements. *Front. Microbiol.* **8**, 1–10 (2017).

9. G. Kimura, E. A. Silver, P. Blum, *Proceedings of the Ocean Drilling Program Initial Reports, Vol. 170* (Ocean Drilling Program, College Station, TX, 1997).

10. A. M. Shaw, D. R. Hilton, T. P. Fischer, J. A. Walker, G. E. Alvarado, Contrasting He-C relationships in Nicaragua and Costa Rica: Insights into C cycling through subduction zones. *Earth Planet. Sci. Lett.* **214**, 499–513 (2003).

11. T. Worzewski, M. Jegen, H. Kopp, H. Brasse, W. Taylor Castillo, Magnetotelluric image of the fluid cycle in the Costa Rican subduction zone. *Nat. Geosci.* **4**, 108–111 (2011).

12. P. H. Barry *et al.*, Forearc carbon sink reduces long-term volatile recycling into the mantle. *Nature*. **568**, 487–492 (2019).

13. M. Crespo-Medina *et al.*, Methane dynamics in a tropical serpentinizing environment: The Santa Elena ophiolite, Costa Rica. *Front. Microbiol.* **8**, 916 (2017).

14. K. Sugimori *et al.*, Microbial life in the acid lake and hot springs of Poás Volcano, Costa Rica. *Colima Volcano Int. Meet.*, 2002 (2002).

15. B. M. Hynek, K. L. Rogers, M. Antunovich, G. Avard, G. E. Alvarado, Lack of Microbial Diversity in an Extreme Mars Analog Setting: Poás Volcano, Costa Rica. *Astrobiology*. **18**, 923–933 (2018).

16. W. F. Giggenbach, Geothermal solute equilibria, derivation of Na-K-Mg-Ca geoindicators. *Geochim. Cosmochim. Acta*. **52**, 2749–2765 (1988).

17. A. Rodríguez, M. J. van Bergen, Superficial alteration mineralogy in active volcanic systems: An example of Poás volcano, Costa Rica. *J. Volcanol. Geotherm. Res.* **346**, 54–80 (2017).

18. F. Tassi *et al.*, The geothermal resource in the guanacaste region (Costa Rica): New hints from the geochemistry of naturally discharging fluids. *Front. Earth Sci.* **6** (2018).

19. M. Yücel, G. W. I. Luther, Temporal trends in vent fluid iron and sulfide chemistry following the 2005/2006 eruption at East Pacific Rise, 9°50′N. *Geochemistry Geophys. Geosystems* (2013).

20. J. M. de Moor *et al.*, Insights on hydrothermal, magmatic interactions, and eruptive processes at Poás Volcano (Costa Rica) from high frequency gas monitoring and drone measurements. *Geophys. Res. Lett.* **46**, 1293–1302 (2019).

21. C. S. Chan, S. C. Fakra, D. Emerson, E. J. Fleming, K. J. Edwards, Lithotrophic iron-oxidizing bacteria produce organic stalks to control mineral growth: Implications for biosignature formation. *ISME J.* **5**, 717–727 (2011).

22. G. R. Hughes, G. A. Mahood, Tectonic controls on the nature of large silicic calderas in volcanic arcs. *Geology*. **36**, 627–630 (2008).

23. M. Protti, F. Gündel, K. McNally, The geometry of the Wadati-Benioff zone under southern Central America and its tectonic significance: results from a high-resolution local seismographic network. *Phys. Earth Planet. Inter.* **84**, 271–287 (1994).

24. M. Watanabe, H. Kojima, M. Fukui, Desulfotomaculum intricatum sp. nov., a sulfate reducer isolated from freshwater lake sediment. *Int. J. Syst. Evol. Microbiol.* **63**, 3574–3578 (2013).

25. J. V. Weiss *et al.*, Characterization of neutrophilic Fe(II)-oxidizing bacteria isolated from the rhizosphere of wetland plants and description of Ferritrophicum radicicola gen. nov. sp. nov., and Sideroxydans paludicola sp. nov. *Geomicrobiol. J.* **24**, 559–570 (2007).

26. S. Nakagawa *et al.*, Sulfurihydrogenibium yellowstonense sp. nov., an extremely thermophilic, facultatively heterotrophic, sulfur-oxidizing bacterium from Yellowstone National Park, and emended descriptions of the genus Sulfurihydrogenibium, Sulfurihydrogenibium subterraneum . *Int. J. Syst. Evol. Microbiol.* **55**, 2263–2268 (2005).

27. L. Hallbeck, K. Pedersen, Autotrophic and mixotrophic growth of Gallionella ferruginea. *J. Gen. Microbiol.* **137**, 2657–2661 (1991).

28. E. V. Odintsova, A. P. Wood, D. P. Kelly, Chemolithoutotrophic growth of Thiothrix ramosa. *Arch. Microbiol.* **160**, 152–157 (1993).

29. S. Douglas, T. J. Beveridge, Mineral formation by bacteria in natural microbial communities. *FEMS Microbiol. Ecol.* **26**, 79–88 (1998).

30. N. R. Hayashi, T. Ishida, A. Yokota, T. Kodama, Y. Igarashi, Hydrogenophilus thermoluteolus gen. nov., sp. nov., a thermophilic, facultatively chemolIthoautotrophic, hydrogen-oxidizing bacterium. *Int. J. Syst. Bacteriol.* **49**, 783–786 (1999).

31. M. S. Kim, S. K. Jo, S. W. Roh, J. W. Bae, Alishewanella agri sp. nov., isolated from landfill soil. *Int. J. Syst. Evol. Microbiol.* **60**, 2199–2203 (2010).

32. W. M. Chen *et al.*, Aquabacterium limnoticum sp. nov., isolated from a freshwater spring. *Int. J. Syst. Evol. Microbiol.* 62, 698–704 (2012).

Material and Methods

All data and code are available through a GitHub repository at the permanent address https://doi.org/10.5281/zenodo.3483104, while the sequencing data is available through the Bioproject accession number SUB6412893 [Avaiting NCBI Confirmation].

Location and Sample Collection. At each sampling site, up to 1.5L of hydrothermal fluids were filtered through Sterivex 0.22 µm filter cartridges (MilliporeSigma), 15mL falcon tubes were filled with sediments and immediately frozen at liquid nitrogen temperature in cryogenic dry shipper (ThermoFisher Scientific, Arctic Express 20) for transport back to the home laboratory. A description of the sites and their GPS coordinates can be found in (*1*). Field sampling for trace metals in the fluids was carried out fixing a filtered sample aliquot in 5% HNO3, whereas for major ions only filtered fluid samples were used. Samples for the determination of trace elements in the solid fraction were sampled in 15 ml falcon tubes and stored frozen. Sediments were also sampled for mineralogical analyses, while samples for scanning electron microscopy where fixed in 3 % formaldehyde and kept at +4°C.

Data for the **carbon isotope analysis** of dissolved inorganic carbon (DIC) and dissolved organic carbon (DOC), the concentration of the sedimentary **aliphatic hydrocarbons** and **polycyclic aromatic hydrocarbons** were previously reported in (*1*) along side the relative methods.

Sedimentary Organic Matter. Total protein, carbohydrate, lipid, chlorophyll-a, and phaeopigments were determined as previously described (*2*). Concentrations were calculated using standard curves, and normalized to sediment dry weight after desiccation (60 ◦ C, 24 h). Protein, carbohydrate, and lipid concentrations were converted into carbon (C) equivalents using the conversion factors of 0.49, 0.40, and 0.75 µgC µg −1, respectively. Chloroplastic pigment equivalents are defined here as the sum of the chlorophyll-a and phaeopigment concentrations.

Geochemistry. Major anions and cations were measured with ion chromatography. Concentrations of anions were determined using a Dionex AS4A-SC separation column, sodium hydroxide eluent and ASRS-I suppressor. For cations a Dionex CS12-SC separation column was used, with methane sulfonic acid eluent and CSRS-I suppressor. Trace metal concentrations were determined in aqueous and acid-digested solid samples with a NexIon 350X ICP-MS instrument. Total acid digestion included microwave-assisted digestion of dry sediments with nitric acid (16N HNO3) and suprapure hydrofluoric acid (HF) and boric acid. The calibration standards were prepared by using Perkin Elmer multi-element calibration standard solution of metals (including Fe, Al, As, Mn, Mg, K, V, Cr, Co, Ni, Ca, Mg, Se, Sr, Ga, Ba, Be, Pb, Cs) in 5% HNO3 with concentration of 10 µg/ml each element. Internal Yttrium standard was added in each sample before analysis to correct the intensity deviations during measurement with ICP-MS. The molar concentrations of each element were calculated by standard calibration curve of each element with multiplication of volume, dilution and division of molar mass.

Flow Cytometry. Samples for cell counts were taken as close to the source spring as possible, usually in an outflow from a rock outcrop or a small surface pool that was rapidly being refilled by the source. We placed 1 ml fluids into a 2 ml plastic tube with a rubber o-ring screwcap (to prevent evaporation) containing 500 µl 3% paraformaldehyde solution in phosphate-buffered-saline (PBS). Cell count samples were kept at room temperature during return to the University of Tennessee and were weighed upon returning to the lab. Cell counts were determined on a Guava Easy Cyte 6HT-2L (Millipore) flow cytometer. Triplicate aliquots of each sample (200µL) were stained with 5× SybrGreen prior to analysis.

Scanning electron microscopy. Scanning electron microscopy (SEM) micrographs of the hydrothermal sediments were obtained on a Phenom ProX scanning electron microscope at 10 and 15 kV and using a charge reduction sample holder. Samples were previously dried at 40°C for 24 hours before imaging, and mounted using conductive carbon tape on a sample pin. The same instrument was used at 15 kV to perform Energy Dispersive X-Ray Spectroscopy (EDX) for elemental analysis of particles in the samples.

X-ray diffraction and Raman spectroscopy. Each sediment sample was dried at 50°C for 24 hours. A representative portion of each sample was ground to <10 um grain size with an alumina mortar and pestle. The ground sample material was analyzed with Bruker D8 powder X-rday diffractomer, with a Cu source (1.5406 nm) and 2-theta range of 5° to 70° at 0.01° increments. Bruker Eva software was used to identify mineral phases with pattern search-match performed on the RRUFF database (http://www.rruff.info/) and AMCSD (http://rruff.geo.arizona.edu/) pattern libraries. Raman spectroscopy was performed on selected samples. The crystals were randomly oriented and the Thermo Almega microRaman system was set at 100% power, using a 532 nm solid-state laser and a thermoelectrically cooled CCD detector. The laser was partially polarized with 4 cm-1 resolution and a spot size of 1 μm. Phase identification was performed using the search-match routines available in the Thermo Almega Omnic and CrystalSleuth software against the RRUFF database Raman spectra library. Trimming and background removal was performed with CrystalSleuth software.

Sequences processing and statistical analysis. Extracted DNA was sequenced for the analysis of the bacterial diversity after amplifying the bacteria-specific V4-V5 region of the 16S rRNA gene using primers 518F (AATTGGANTCAACGCCGG) and B1048R (CGTCTGCCATGYACCWC). Sequencing was performed has part of the Census of Deep Life initiative with the Deep Carbon Observatory and performed at the Marine Biological Laboratory sequencing facility (https://www.mbl.edu/) on an Illumina platform. Obtained reads were processed using mothur (*3*), following the Miseq standard operating procedure. Taxonomy was assigned using the RDP naive bayesian classifier against the Silva v132 release (*4*).

All statistical analyses, data processing and plotting where carried out in the R statistical software (*5*), using the phyloseq (*6*), vegan (*7*), ggtern (*8*), missForest (*9*), VSURF (*10*) and ggplot2 (*11*) packages. A complete R scrip containing all the step to reproduce our analysis is available at https://github.com/dgiovannelli/SubductCR_16S-diversity.git and released as a permanent version using Zenodo under the DOI: https://doi.org/10.5281/zenodo.3483104. Briefly, obtained count table, taxonomy assignment and phylogenetic tree were combined together with the environmental variables into a *phyloseq* object. Low prevalence ASVs, mitochondria and chloroplast related sequences and potential contaminants were removed (Fig. S9). In both fluids and sediments, common laboratory contaminants from DNA processing, feces, and skin (Sheik et al. 2018) were largely absent (< 0.04% in the entire dataset and less than 0.01% in any individual library), and no ASV was shared by all samples. *Acinetobacter* sp., a group containing hospital-acquired pathogens as well as environmental clades (14), was in high abundance (between 20 and 60% of the reads) in three samples of hydrothermal water collected in spas/resorts, and was removed from further analysis. The remaining ASVs represented the ~81% of the original reads. In total 1,933,379 reads and 33,188 ASVs were retained after the preprocessing steps.

Obtained results were used for diversity plots and for multivariate analysis. The basic approach involved non-metric multidimensional scaling (nMDS) using Jaccard and Unifrac distances (the latter both weighted and unweighted) to identify similarity in bacterial diversity community composition across the sampled stations as previously described (*12*, *13*). nMDS ordinations were used to identify potential environmental explanatory variables using linear correlations of environmental vectors with the envfit function in vegan. The role of different sampling factors in influencing the observed community patterns were tested using a permutation distance based approach using the adonis function of the vegan package. Tested factors included the sample matrix type (*type*: fluids, sediments), the subducting plate (*plate*: EPR or CNS), the location of the sampling site along the volcanic arc (*province*: outer forearc, forearc, arc), the geological province based on the map reproduced in Figure 1 (*geol_prov*: 1, 2, 3 and 4), dominant basement rock type obtained from the USGS Mineral Resources GIS maps (*14*) (*rocks*), the volcanic area the sampling sites is located in (*volcano*: forearc and the name of the major Costa Rica volcanoes). Additionally, two factors (*anions* and *cations*) were obtained based on the ternary plot of the aqueous geochemical composition of the fluids at each site as presented in Figure 2b and 2c. The sampled sites were classified using their position in these plots, based on their geochemical composition, their interaction with different underlying basement rocks and the degree of equilibration according to Giggenbach (*15*, *16*).

Dominant ASVs were obtained by adding a further step of prevalence filtering, removing all the ASVs with a global abundance of less than 20 reads and present in at least 3 samples. This step reduced the number of ASVs to about 12% of the original variants, while retaining ~73% of the total reads. The diversity plots were inspect to ensure that no major changes in the dominant phylotypes and taxonomic groups were introduced (Supplementary Figure S8 comparison_filtering). At this step PL was removed from the dataset because it was the only sample representing a hyperacidic volcanic crater lake. A co-occurrence network was constructed based on pairwise Spearman rank correlations among the ASVs across the entire dataset. Only positive correlations with a Spearman's correlation coefficient (ρ) > 0.65 were retained, as they provide information on microbial phylotypes that may respond similarly to environmental conditions. The network we recovered included 3,935 nodes with 339,803 edges. The topology of the obtained network was investigated and a modularity analysis using a number of clustering algorithms built in the R package igraph (*17*) was performed (random walks, label propagation and Louvain clustering algorithms). While the total number of clusters changed, the main clusters identified by the tested algorithms converged, and the top 10 clusters were identified by the Louvain clustering algorithms. Identified clusters represented ecological cliques of phylotypes showing a cohesive behavior across the sampled hot springs. The cumulative abundance of all the phylotypes belonging to each clique was correlated using both Pearson moment correlation and Spearman rank correlation against all the environmental predictors. A conservative p level of $p<0.01$ was selected for all statistical tests performed (*18*). The relationship between each clique cumulative abundance and environmental predictors was also manually inspected using scatterplots, to identify possible non-linear relationships and confirm correlations identified with statistical testing. To further test the validity of the identified environmental predictors in explaining each clique distribution we performed a Random Forests (RF) regression analysis for the identification of environmental variable importance. The analysis was carried out using the VSURF package. Clique abundances were re-scaled using z-scores before the RF analysis and missing environmental observations were imputed using the missForest package. The variables identified by each different approach (scatterplots inspection, Pearson moment correlation, Spearman rank correlation and RF analysis) overlapped significantly. The most informative environmental variable associated with the distribution of each clique was selected for plotting in Figure 4b.

Methods References

1. P. H. Barry, J. M. de Moor, D. Giovannelli, M. Schrenk, D. R. Hummer, T. Lopez, C. A. Pratt, Y. A. Segura, A. Battaglia, P. Beaudry, G. Bini, M. Cascante, G. d'Errico, M. di Carlo, D. Fattorini, K. Fullerton, E. Gazel, G. González, S. A. Halldórsson, K. Iacovino, J. T. Kulongoski, E. Manini, M. Martínez, H. Miller, M. Nakagawa, S. Ono, S. Patwardhan, C. J. Ramírez, F. Regoli, F. Smedile, S. Turner, C. Vetriani, M. Yücel, C. J. Ballentine, T. P. Fischer, D. R. Hilton, K. G. Lloyd, Forearc carbon sink reduces long-term volatile recycling into the mantle. *Nature*. **568**, 487 (2019).

2. D. Giovannelli, G. d'Errico, F. Fiorentino, D. Fattorini, F. Regoli, L. Angeletti, T. Bakran-Petricioli, C. Vetriani, M. Yücel, M. Taviani, E. Manini, Diversity and Distribution of Prokaryotes within a Shallow-Water Pockmark Field. *Front. Microbiol.* **7** (2016), doi:10.3389/fmicb.2016.00941.

3. P. D. Schloss, S. L. Westcott, T. Ryabin, J. R. Hall, M. Hartmann, E. B. Hollister, R. A. Lesniewski, B. B. Oakley, D. H. Parks, C. J. Robinson, J. W. Sahl, B. Stres, G. G. Thallinger, D. J. Van Horn, C. F. Weber, Introducing mothur: open-source, platform-independent, community-supported software for describing and comparing microbial communities. *Appl. Environ. Microbiol.* **75**, 7537–7541 (2009).

4. C. Quast, E. Pruesse, P. Yilmaz, J. Gerken, T. Schweer, P. Yarza, J. Peplies, F. O. Glöckner, The SILVA ribosomal RNA gene database project: improved data processing and web-based tools. *Nucleic Acids Res.* **41**, D590–D596 (2013).

5. R. development Core Team, R: A Language and Environment for Statistical Computing. (2010), (available at http://www.R-project.org).

6. P. J. McMurdie, S. Holmes, phyloseq: An R Package for Reproducible Interactive Analysis and Graphics of Microbiome Census Data. *PLOS ONE*. **8**, e61217 (2013).

7. J. Oksanen, F. G. Blanchet, R. Kindt, P. Legendre, P. R. Minchin, R. B. O'Hara, G. L. Simpson, P. Solymos, Stevens, H. Wagner, vegan: Community Ecology Package. *R Package Version 20-7* (2012) (available at http://CRAN.R-project.org/package=vegan).

8. N. E. Hamilton, M. Ferry, ggtern: Ternary Diagrams Using ggplot2. *J. Stat. Softw.* **87**, 1–17 (2018).

9. D. J. Stekhoven, P. Bühlmann, MissForest—non-parametric missing value imputation for mixed-type data. *Bioinformatics*. **28**, 112–118 (2012).

10. R. Genuer, J.-M. Poggi, C. Tuleau-Malot, VSURF: An R Package for Variable Selection Using Random Forests. *R J.* **7**, 19–33.

11. H. Wickham, *ggplot2: Elegant Graphics for Data Analysis* (Springer-Verlag, New York, 2009; https://www.springer.com/gp/book/9780387981413), *Use R!*

12. D. Giovannelli, M. Molari, G. d'Errico, E. Baldrighi, C. Pala, E. Manini, Large-Scale Distribution and Activity of Prokaryotes in Deep-Sea Surface Sediments of the Mediterranean Sea and the Adjacent Atlantic Ocean. *PLoS ONE*. **8**, e72996 (2013).

13. D. Giovannelli, G. d'Errico, E. Manini, M. M. Yakimov, C. Vetriani, Diversity and phylogenetic analyses of bacteria from a shallow-water hydrothermal vent in Milos island (Greece). *Front. Extreme Microbiol.* **4**, 184 (2013).

14. P. G. Schruben, "Geology and resource assessment of Costa Rica," *U.S. Geological Survey Digital Data Series DDS-19-R*, (available at https://mrdata.usgs.gov/dds-19/).

15. W. F. Giggenbach, Geothermal solute equilibria. Derivation of Na-K-Mg-Ca geoindicators. *Geochim. Cosmochim. Acta*. **52**, 2749–2765 (1988).

16. W. F. Giggenbach, R. C. Soto, Isotopic and chemical composition of water and steam discharges from volcanic-magmatic-hydrothermal systems of the Guanacaste Geothermal Province, Costa Rica. *Appl. Geochem.* **7**, 309–332 (1992).

17. G. Csardi, T. Nepusz, The igraph software package for complex network research. *InterJournal Complex Syst.* **1695**, 1–9 (2006).

18. A. Underwood, Beyond BACI: experimental designs for detecting human environmental impacts on temporal variations in natural populations. *Mar. Freshw. Res.* **42**, 569–587 (1991).

Figures

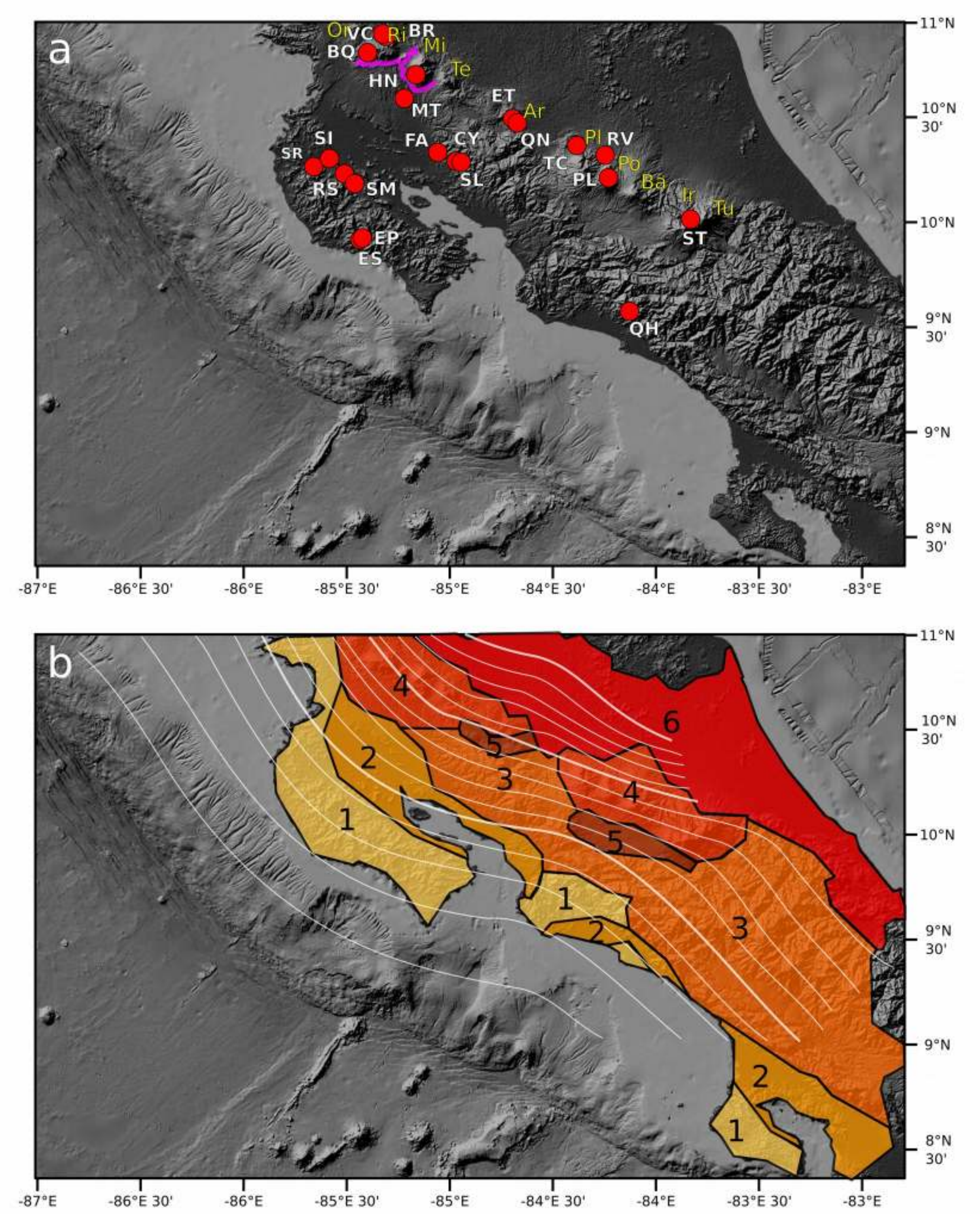

Figure 1. **Sampling sites were distributed along a transect across the Costa Rica convergent margin** – location of the sampled hot springs and volcano lake (red dots with white station labels), the location of the volcano chain (yellow labels) and the Guanacaste Geothermal Province caldera structures (purple lines, adapted from Tassi et al., 2018). b – overlay of the subducting slab depth lines (thin lines every 10 km depth, thick lines every 50 km depth) and the principal type of bedrocks found in the area. Volcanoes (yellow labels): Or – Orosi; Ri – Rincón de la Vieja; Mi – Miravalles; Te – Tenorio; Ar – Arenal; Pl – Platanar; Po – Poás; Ba – Barva; Ir – Irazú; Tu – Turrialba. Geological map (adapted from Tassi et al., 2004): 1 – Createceous-Tertiary ophiolites; 2 – Tertiary basins; 3 – Tertiary volcanic range; 4 – Quaternary volcanic range; 5 – Intra-arc basins; 6- Carribean coastal plain

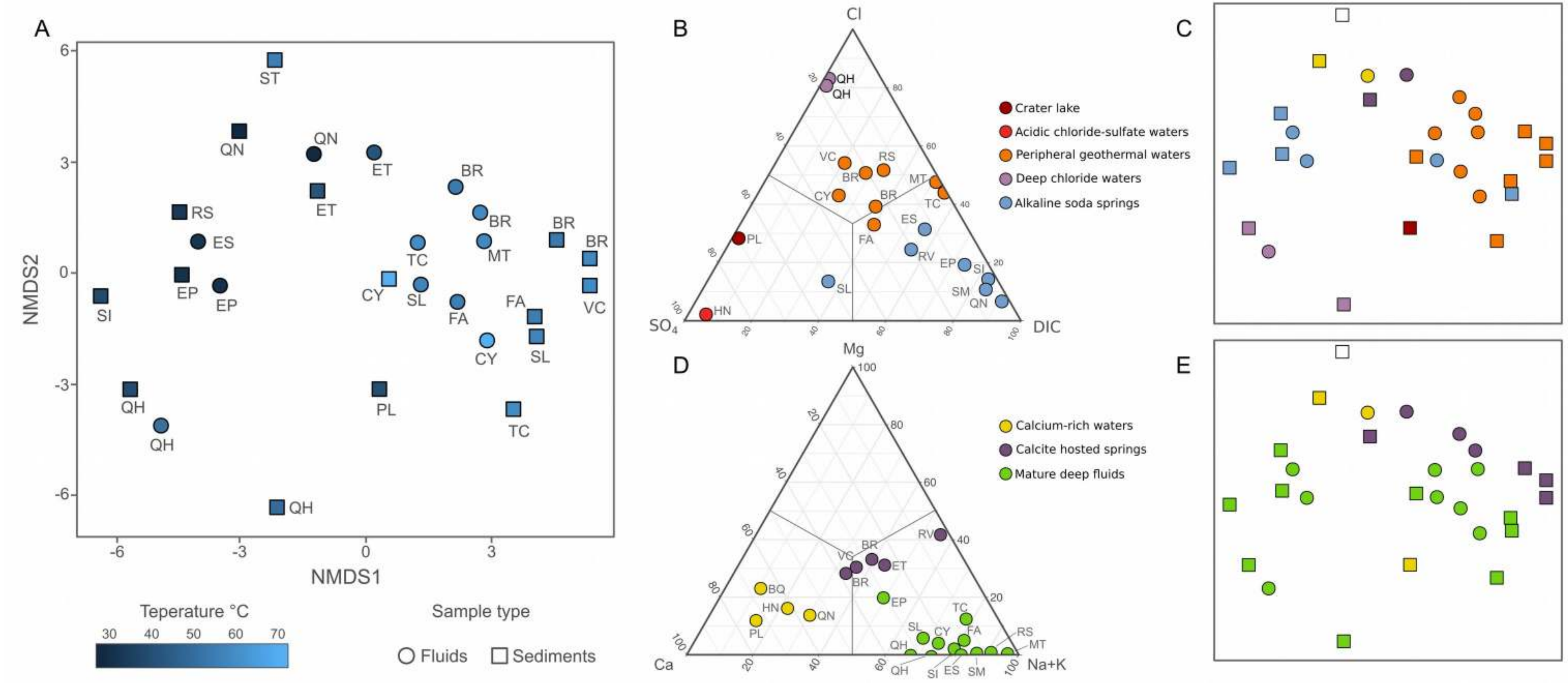

Figure 2. **Total bacterial community composition changes along with deep subsurface geochemistry.** A – Weighted non-metric multi dimensional scaling (nMDS) plot of the microbial diversity based on Jaccard dissimilarity measure in the fluids (circles) and sediments (squares) of the sampled hot springs across the Costa Rica volcanic arc, colored by spring temperature; B and D – Ternary diagram showing the clustering of the sampled hot springs based on the major anions (B) and major cations (C). The samples have been colored according to their position in the plots, and interpreted as reported in the main text; C and E – nMDS plot showing the same results presented in A, but colored according to the geochemistry-based grouping extracted from B and D respectively. Cation and anion data were not available for site ST.

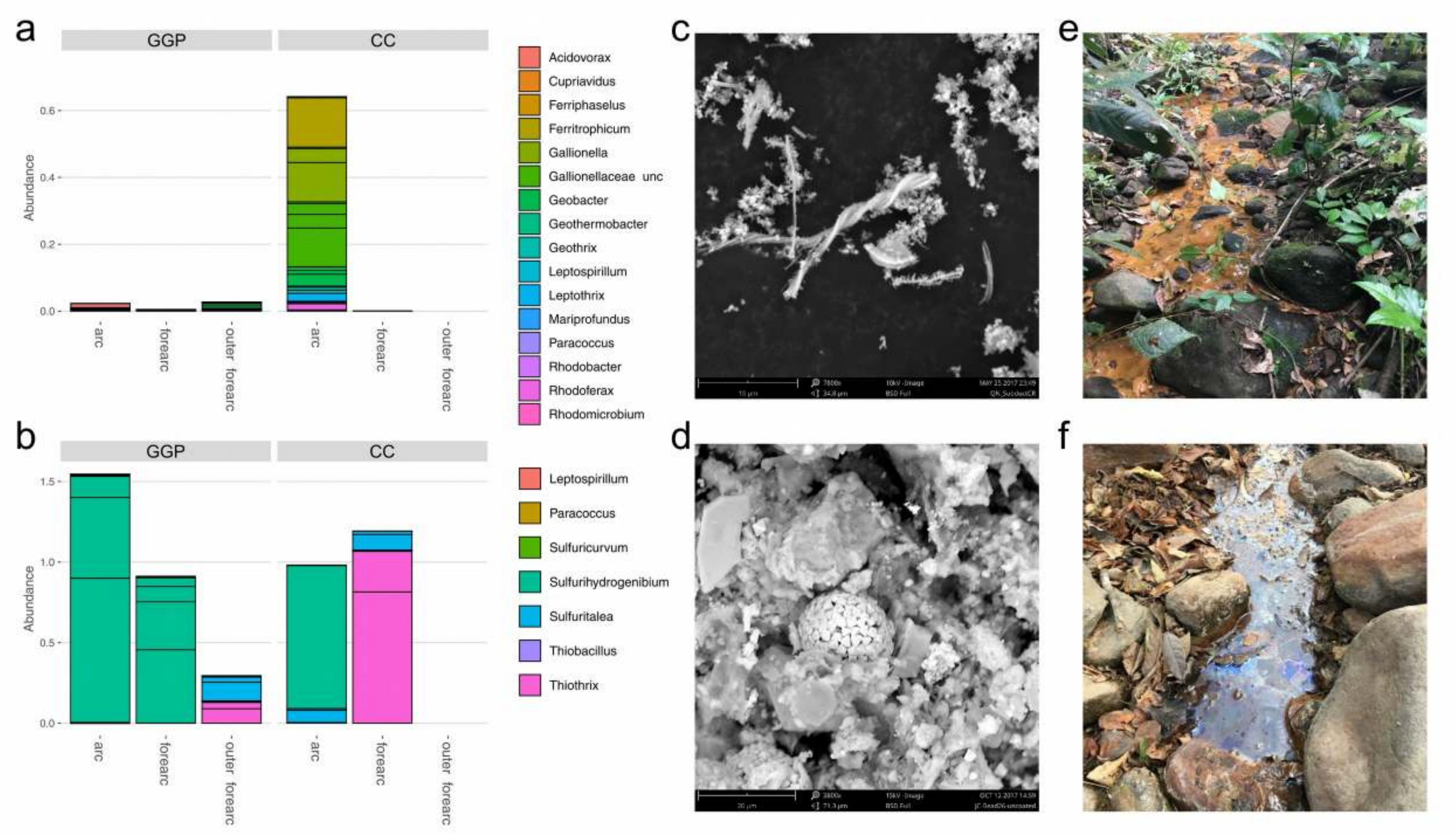

Figure 3. Bacterial sulfur oxidation occurs throughout the forearc/arc, whereas iron oxidation occurs only in the central CNS plate. Relative cumulative abundance of putative iron (A) and sulfur (B) oxidizing genera across the sites corresponding to the two subducting plates with sites grouped according to the arc province (arc, forearc, outer forearc) and the two plates (the East Pacific Rise in north Costa Rica and the Nazca-Cocos Spreading center in central-south Costa Rica). Note the difference in abundance scale (%) between the two plots. Lines drawn within a single box color represent contributions from different samples. Representative photographs of lack of largescale iron hydroxide deposits in the northern site San Lucia, SL (C) and presence of them in the central site Quebrada Naranja, QN (F). Scanning electron micrographs show pyrite framboids at SL (D) and twisted stalks of iron hydroxides deposited by iron oxidizing bacteria at QN (E).

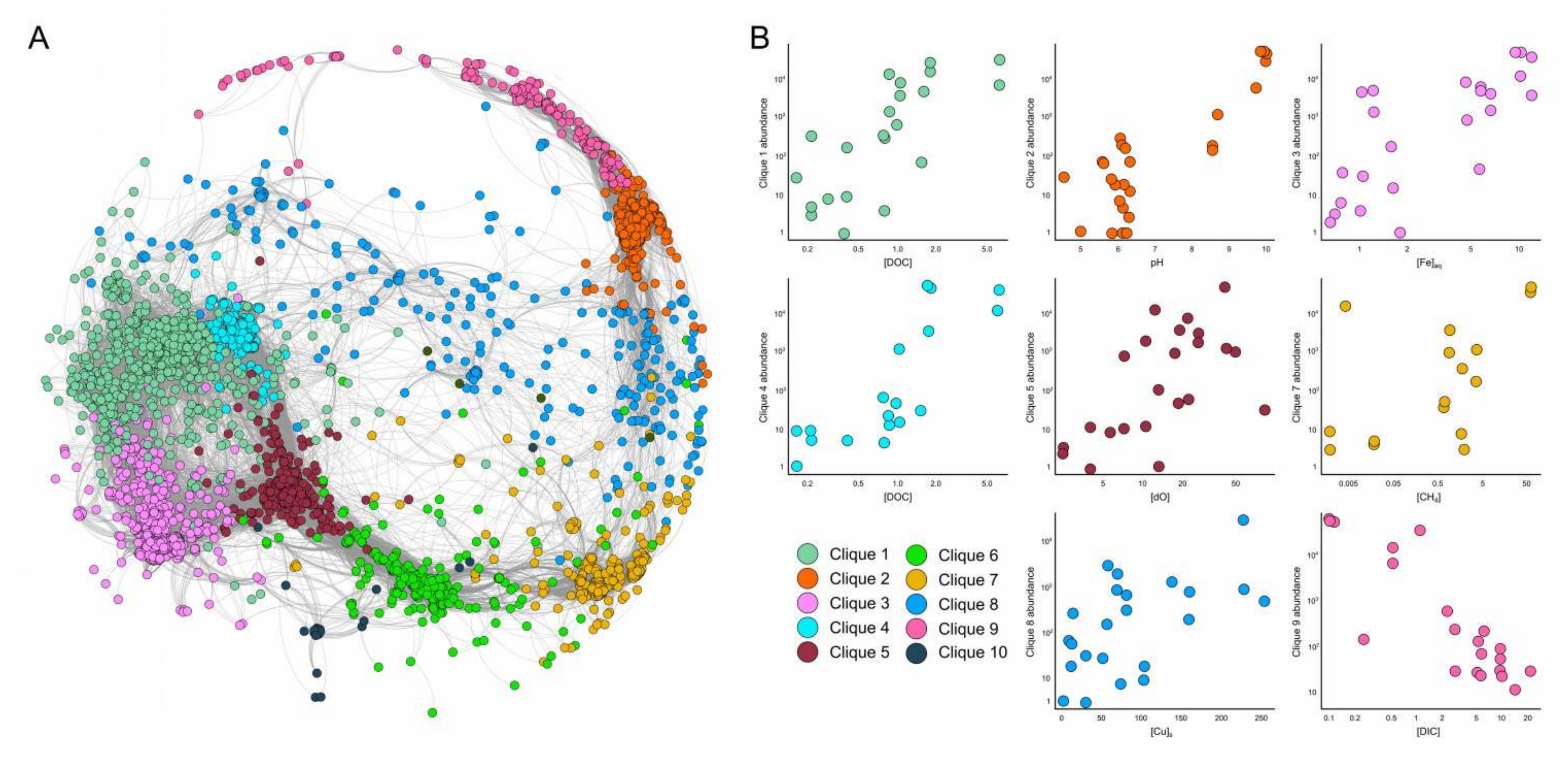

Figure 4. Bacterial subgroups have unique relationships to subduction zone geochemistry. A) Co-occurrence network of the dominant phylotypes in the hot-spring samples colored according to the assigned clique. Only positive Spearman correlations above 0.65 have been plotted as edges; B) Combined abundance of the phylotypes present in each clique plotted against the environmental variables identified by the correlation approach as the major explanatory variables for that clique.

Supplementary Tables

Table S1. Results of flow cytometry cell counts of subsurface geothermal fluids, divided by A) province across the subduction zone, and B) EPR (Northern) vs CNS (Southern) plates.

Site	n	Average (cells/mL)	Standard Deviation (cells/mL)
BQ	3	1.058×10^6	1.145×10^5
BR1	3	1.103×10^6	3.786×10^4
BR2	3	1.200×10^6	8.185×10^4
ES	3	2.780×10^4	7.104×10^3
ET	3	5.157×10^4	3.418×10^4
FA	3	1.307×10^6	1.320×10^5
HN	3	2.613×10^6	1.656×10^5
MT	3	7.550×10^4	1.230×10^4
PL	6	2.392×10^3	1.550×10^4
QH1	3	3.043×10^6	4.283×10^5
QN	3	1.863×10^5	4.725×10^4
RS	3	3.607×10^5	6.688×10^4
RV	3	1.374×10^6	7.210×10^5
SG	3	3.568×10^4	2.308×10^4
SI	3	1.876×10^4	1.072×10^4
SR	3	1.076×10^6	1.659×10^5
ST	3	6.383×10^5	1.326×10^5
TC	3	1.720×10^5	5.534×10^4
VC	3	2.320×10^6	3.704×10^5

Table S2. Results of ADONIS analysis on the environmental factors explaining the variance in the nMDS ordination obtained from the 16S rRNA diversity. *Type* – sample source (fluids – sediments); *Plate* – Sites corresponding to the projection of plate subduction of the East Pacific Rise and the Cocos-Nazca Spreading center; *Province* – Division in region along the volcanic arc in outer forearc, forearc and arc; *Geol_prov* – Geological province as defined by the principal types of bedrocks (figure 1); *Rocks* – Primary rock types found at each location extracted from the Macrostrat database; *Volcano* – Different volcanic provinces; *Anions* – factor highlighting the different groups in the geochemical ternary plot presented in Figure 2B; *Cations* – factor highlighting the different groups in the geochemical ternary plot presented in Figure 2C. Interaction factors are also reported for the factors nested in type (i.e., type:N tests of variable N were performed on sediments or fluids separately).

Factor	**df**	**r^2**	***p***	**sign.**
type	1	0.044	0.016	*
plate	**1**	**0.055**	**0.001**	***
province	**2**	**0.125**	**0.001**	***
region	**1**	**0.045**	**0.008**	**
geol_prov	**1**	**0.048**	**0.002**	**
rocks	3	0.109	0.078	.
volcano	**2**	**0.081**	**0.004**	**
anions	1	0.032	0.653	
cations	**1**	**0.043**	**0.001**	***
type:plate	1	0.031	0.769	
type:province	2	0.061	0.864	
type:region	1	0.032	0.700	
type:geol_prov	1	0.031	0.774	
type:rocks	1	0.035	0.341	
type:anions	1	0.027	0.967	

Table S3. Results of the linear vector fitting onto the nMDS ordination of the 16S rRNA bacterial diversity. NMDS based on Jaccard diversity obtained using the Vegan package (Oksanen et al., 2012). Environmental variables with a $p<0.01$ are highlighted in bold. The type of samples on which the measurements were made are listed next to the variable name; options are hot spring fluids collected as close as possible from the expression orifice (fluids), surface sediments being overwashed by hot spring fluids (sed), and gas bubbles collected by a funnel and Giggenbach bottle (gas).

Variable	**NMDS1**	**NMDS2**	**r^2**	***p***	**sign.**
alt	0.26233	0.96498	0.342	0.0824	.
Temperature	**-0.99051**	**-0.13744**	**0.567**	**0.0075**	**
Barometric pressure	-0.2524	-0.96762	0.326	0.0929	.
Dissolved oxygen	0.89051	0.45496	0.016	0.9112	
Specific conductivity	-0.75268	-0.65838	0.363	0.0650	.
pH	**0.75543**	**-0.65523**	**0.679**	**0.0011**	**
fnu	-0.99812	-0.06123	0.483	0.0178	*
hum	0.58101	-0.8139	0.051	0.7295	
temp_amb	-0.99087	-0.13483	0.072	0.6278	
Dissolved inorganic carbon (DIC), fluids	**-0.95008**	**0.3120**	**0.513**	**0.0024**	**
δ^{13}C of DIC, fluids	**-0.98901**	**0.14787**	**0.500**	**0.0022**	**
Dissolved organic carbon (DOC), fluids	-0.92826	0.37194	0.231	0.0897	.
δ^{13}C of DOC, fluids	**-0.84191**	**0.53961**	**0.744**	**0.0002**	***
Total organic carbon (TOC), sed	0.34798	-0.9375	0.181	0.1606	
δ^{13}C of TOC, sed	-0.36883	-0.9295	0.114	0.3317	
Total carbon (TC), sed	0.15959	-0.98718	0.238	0.0853	.
δ^{13}C of TC, sed	-0.90865	-0.41757	0.180	0.1600	
Total nitrogen (TN), sed	**0.27543**	**-0.96132**	**0.430**	**0.0053**	**
δ^{15}N of TN, sed	**-0.19806**	**0.98019**	**0.685**	**0.0001**	***
CO$_2$, gas	-0.87387	0.48615	0.181	0.4228	
He, gas	-0.22943	-0.97333	0.086	0.6649	
H$_2$, gas	0.77179	-0.63588	0.145	0.4837	
O$_2$, gas	0.39602	-0.91824	0.316	0.1744	
Ar, gas	-0.03274	-0.99946	0.409	0.0922	.
N$_2$, gas	-0.07481	-0.9972	0.354	0.1419	
CH$_4$, gas	0.87714	0.48023	0.733	0.0159	*
δ^{13}C of CO$_2$, gas	0.99413	-0.10822	0.014	0.9392	
Rc/Ra, gas	-0.98615	0.16584	0.029	0.9040	
X-value, a measure of air contamination on He isotopes, gas	-0.88139	0.47239	0.226	0.3155	
CO$_2$/He^3, gas	-0.8247	0.56557	0.072	0.7343	
Low molecular weight polyaromatic hydrocarbons (PAH), sed	0.30156	0.95345	0.033	0.7399	
High molecular weight PAH, sed	-0.9251	0.37973	0.039	0.7015	
Total PAH, sed	-0.84268	0.53842	0.030	0.7554	

Aliphatic hydrocarbons, sed	-0.98894	-0.1483	0.200	0.1205	
Proteins, sed	-0.25251	0.96759	0.272	0.0865	.
Charbohydrates, sed	-0.43069	0.9025	0.324	0.0512	.
Lipids, sed	-0.9744	-0.22484	0.089	0.4949	
cha	**0.51266**	**-0.85859**	**0.458**	**0.0083**	**
Feo pigments, sed	-0.35086	0.93643	0.239	0.1143	
cpe	0.61308	-0.79002	0.302	0.0570	.
Al (acidified), fluid	**0.9947**	**0.10284**	**0.357**	**0.0060**	**
Cr (acidified), fluid	**0.147**	**0.98914**	**0.396**	**0.0038**	**
Mn (acidified), fluid	-0.96863	-0.2485	0.261	0.0323	*
Fe (acidified), fluid	**-0.64156**	**-0.76707**	**0.601**	**0.0001**	***
Ni (acidified), fluid	**-0.66018**	**-0.75111**	**0.639**	**0.0001**	***
Cu (acidified), fluid	-0.80466	-0.59374	0.307	0.0148	*
zn_ac	**-0.95129**	**0.3083**	**0.574**	**0.0001**	***
Cd (acidified), fluid	-0.97645	0.21574	0.235	0.0449	*
Ag (acidified), fluid	-0.7925	-0.60987	0.023	0.7707	
Co (acidified), fluid	0.15432	0.98802	0.195	0.0850	.
F, fluid	0.29924	-0.95418	0.413	0.0870	.
Cl, fluid	**-0.54528**	**-0.83825**	**0.659**	**0.0095**	**
SO_4, fluid	-0.71781	-0.69624	0.550	0.0344	*
H_2S, fluid	0.97664	-0.21488	0.397	0.0685	.
Br, fluid	-0.59381	-0.8046	0.496	0.0484	*
NO_3^-, fluid	0.55405	-0.83248	0.077	0.6792	
PO_4^{3-}, fluid	**-0.91577**	**0.4017**	**0.892**	**0.0001**	***
Li^+, fluid	-0.99296	0.11844	0.252	0.2669	
Na^+, fluid	-0.7928	-0.60949	0.271	0.2363	
NH_4^+, fluid	-0.74426	0.66788	0.184	0.3976	
K^+, fluid	-0.74267	-0.66965	0.664	0.0103	*
Mg^{2+}, fluid	-0.62999	-0.77661	0.476	0.0519	.
Ca^{2+}, fluid	**-0.51589**	**-0.85665**	**0.698**	**0.0069**	**
Si, fluid	-0.87463	0.4848	0.401	0.1035	
al_s	**0.368**	**0.92983**	**0.460**	**0.0020**	**
cr_s	**0.95039**	**-0.31108**	**0.625**	**0.0001**	***
mn_s	-0.24201	0.97027	0.17	0.1333	
fe_s	-0.76045	-0.6494	0.281	0.0318	*
ni_s	**0.99843**	**0.056**	**0.544**	**0.0004**	***
cu_s	**0.26919**	**0.96309**	**0.359**	**0.0092**	**
zn_s	-0.48359	0.8753	0.169	0.1383	
cd_s	0.26455	0.96437	0.150	0.1748	
ag_s	0.33602	0.94185	0.244	0.0514	.

Table S4. Table showing the results of the Pearson moment correlation analysis between the nMDS ordination dimension 1 and 2 (based on Jaccard similarity index) and the environmental variables. Only variables with a $p<0.01$ are highlighted in bold.

	NMDS1			**NMDS2**		
variable	**r^2**	**df**	***p***	**r^2**	**df**	***p***
temperature	**-0.750**	**25**	**6.58E-06**	-0.194	25	0.331
ph	**0.710**	**25**	**3.34E-05**	-0.353	25	0.070
[DIC]	**-0.680**	**21**	**3.37E-04**	0.227	21	0.298
DIC-δ^{13}C	**-0.702**	**21**	**1.87E-04**	0.122	21	0.579
DOC-δ^{13}C	**-0.795**	**21**	**5.95E-06**	0.337	21	0.116
[TN]	0.292	23	0.157	**-0.598**	**23**	**1.59E-03**
TN-δ^{15}N	-0.262	23	0.207	**0.820**	**23**	**5.16E-07**
Chl-a	0.478	18	0.033	-0.283	18	0.227
[Al]$_{aq}$	**0.596**	**24**	**1.30E-03**	0.004	24	0.983
[Cr]$_{aq}$	0.108	24	0.601	**0.612**	**24**	**8.79E-04**
[Fe]$_{aq}$	**-0.605**	**24**	**1.06E-03**	-0.448	24	0.022
[Ni]$_{aq}$	**-0.637**	**24**	**4.71E-04**	-0.446	24	0.023
[Zn]$_{aq}$	**-0.742**	**24**	**1.41E-05**	0.195	24	0.338
[Cl]	**-0.594**	**24**	**1.39E-04**	-0.466	24	0.017
[PO$_4$]	**-0.532**	**24**	**5.11E-03**	0.427	24	0.029
[Ca]	**-0.557**	**24**	**3.10E-03**	**-0.573**	**24**	**2.24E-03**
[Al]$_s$	0.402	22	0.052	**0.554**	**22**	**4.96E-03**
[Cr]$_s$	**0.778**	**22**	**7.62E-06**	-0.126	22	0.556
[Ni]$_s$	**0.737**	**22**	**3.96E-05**	0.037	22	0.864
[Cu]$_s$	0.270	22	0.188	**0.536**	**22**	**6.922E-03**
FNU	0.004	20	0.985	0.401	20	0.065
[CH$_4$]	0.221	17	0.363	0.423	17	0.071
[K]$_{aq}$	**-0.745**	**24**	**1.26E-05**	-0.188	24	0.358

Table S5. clique_composition. Genus taxonomic assignment of the ASV with cumulative abundance calculated within the clique above 1%. The ASV cumulative abundance within each clique is reported in bold.

Cliques					
Clique 1		**Clique 2**		**Clique 3**	
Genus	**Abund.**	**Genus**	**Abund.**	**Genus**	**Abund.**
Chloroflexus	8.39%	Hydrogenophilaceae_uncultured	12.34%	Bacteria_unclassified	19.76%
Firmicutes_unclassified	7.37%	Nitrospirae_uncultured_ge	8.67%	*Meiothermus*	9.77%
Chloroflexi_uncultured	4.88%	Bacteria_unclassified	8.62%	Firmicutes_unclassified	7.61%
Sulfurihydrogenibium	4.66%	SBR1031_ge	5.56%	SM1H02_ge	5.32%
Bacteria_unclassified	4.53%	*Desulfatirhabdium*	5.32%	Nitrospirae_uncultured_ge	5.15%
SJA-15_ge	4.45%	Sva0485_ge	4.92%	Clostridia_unclassified	4.79%
Betaproteobacteriales_unclassified	4.33%	GIF9_ge	4.75%	Sulfurihydrogenibium	3.07%
vadinHA49_ge	4.03%	Syntrophaceae_unclassified	4.51%	*Chloroflexus*	3.01%
Thermoanaerobaculum	3.92%	Ignavibacteria_unclassified	3.38%	Rhodocyclaceae_unclassified	2.74%
Rhodocyclaceae_unclassified	3.83%	Desulfobacteraceae_unclassified	2.91%	GAL15_ge	2.47%
Armatimonadetes_uncultured_ge	3.52%	GAL15_ge	2.00%	*Methylothermus*	2.33%
Thermus	3.35%	BSV26_ge	1.68%	Clostridiales_unclassified	2.32%
OPB56_ge	3.20%	Lentimicrobiaceae_ge	1.55%	Planctomycetes_uncultured	2.30%
Bacteroidia_unclassified	2.80%	UTCFX1	1.42%	Deltaproteobacteria_unclassified	1.85%
Gaiellales_unclassified	2.64%	OPB41_ge	1.37%	Armatimonadetes_uncultured_ge	1.78%
Pirellulaceae_unclassified	2.44%			Candidatus_Alysiosphaera	1.73%
Hydrogenophilus	2.32%			11-24_ge	1.24%
Nitrospirae_uncultured_ge	2.01%			Chloroflexi_unclassified	1.16%
SM1H02_ge	1.96%			Chthonomonadales_ge	1.06%
Pedosphaeraceae_unclassified	1.54%			Solibacteraceae__unclassified(100)	1.03%
11-24_ge	1.03%			S085_ge	1.03%
Xanthomonadaceae_uncultured	1.00%			Chloroflexi_uncultured	1.01%
Clique ASV cumulative abundance	**78.20%**		**69.00%**		**82.53%**

Clique 4		**Clique 5**		**Clique 6**	
Genus	**Abund.**	**Genus**	**Abund.**	**Genus**	**Abund.**
Sulfurihydrogenibium	55.03%	*Tepidimonas*	95.81%	*Aquabacterium*	46.36%
Hydrogenothermaceae_unclassified	9.64%	*Anoxybacillus*	1.56%	*Alishewanella*	21.85%
Hydrogenophilus	4.90%	*Caldimonas*	1.52%	*Vogesella*	9.91%
Meiothermus	4.46%			*Rheinheimera*	9.18%
Rhodothermus	3.33%			*Exiguobacterium*	4.76%
Bacteria_unclassified	3.24%			*Novosphingobium*	1.07%
Thermus	2.81%				
Thermobrachium	2.73%				
Thermoleophilum	2.40%				
Thermodesulforhabdus	2.37%				
Thermodesulfovibrio	1.28%				
OPB56_ge	1.14%				
Clique ASV cumulative abundance	**93.34%**		**98.89%**		**93.13%**

Clique 7		**Clique 8**		**Clique 9**	
Genus	**Abund.**	**Genus**	**Abund.**	**Genus**	**Abund.**
Chloroflexi_uncultured	10.10%	Leptolyngbyaceae_unclassified	14.96%	*Thiothrix*	65.70%
Prevotella_9	8.98%	JdFR-76	10.94%	Hydrogenophilaceae_uncultured	11.33%

Acidovorax	8.24%	*Nitrospira*	6.49%	*Sulfuritalea*	7.90%
Gallionella	7.73%	Chloroflexi_uncultured	5.09%	*Lentimicrobium*	2.32%
TPD-58	6.48%	Burkholderiaceae_unclassified	4.54%	Armatimonadetes_uncultured_ge	1.61%
Enterobacteriaceae_unclassified	5.99%	*Nitrosomonas*	3.94%	*Desulfotomaculum*	1.28%
MBNT15_ge	5.86%	Subgroup_6_ge	3.90%	*Thiobacillus*	1.27%
Rhodocyclaceae_unclassified	3.90%	Anaerolineaceae_unclassified	3.62%	Blvii28_wastewater-sludge_group	1.07%
Dechloromonas	3.82%	TRA3-20_ge	2.90%		
Burkholderiaceae_unclassified	3.49%	RCP2-54_ge	2.43%		
Geobacter	2.73%	UTCFX1	1.99%		
Sulfuritalea	2.50%	WD2101_soil_group_ge	1.43%		
Spirochaetaceae_uncultured	2.14%	Hydrogenophilaceae_uncultured	1.35%		
Thermus	2.01%	*Pedomicrobium*	1.31%		
Methylocystis	1.94%	Fimbriimonadaceae_ge	1.27%		
Anaerolineaceae_unclassified	1.71%	Gaiellales_unclassified	1.23%		
Ferriphaselus	1.35%	Blastocatellaceae_unclassified	1.15%		
SR-FBR-L83_ge	1.07%	*Pirellula*	1.15%		
Novosphingobium	1.05%	Gaiellales_uncultured_ge	1.03%		
Clique ASV cumulative abundance	**81.08%**		**70.75%**		**92.47%**

Clique 10	
Genus	**Abund.**
Sulfurihydrogenibium	93.81%
Gammaproteobacteria_uncultured	2.06%
Clique ASV cumulative abundance	**95.88%**

Table S6. Results of the Pearson moment correlation between the cumulative abundance of the ASVs in each clique and environmental variables. Only correlations with p<0.01 are highlighted in bold.

Cliques	Factor	r2	df	p
Clique 1	**doc**	0.65	21	0.0008
	doc_d13	0.59	21	0.0029
	co2_he3	0.77	16	0.0002
	ah	0.56	20	0.0067
	so4	0.69	24	0.0001
	po4	0.58	24	0.0018
	li	0.71	24	4.44E-05
	na	0.61	24	0.0011
	nh4	0.67	24	0.0002
	zn_s	0.74	22	4.04E-05
Clique 2	**temp**	-0.53	25	0.0043
	ph	0.76	25	4.58E-06
	dic_d13	-0.59	21	0.0029
	co2	-0.68	17	0.0013
	h2	0.73	17	0.0004
	o2	0.71	17	0.0006
	ar	0.90	17	1.07E-07
	n2	0.98	17	1.47E-12
	al_ac	0.84	24	6.10E-08
	cl	-0.53	24	0.0056
	cr_s	0.67	22	0.0004
	ni_s	0.76	22	1.86E-05
Clique 3	**spc**	0.51	25	0.0065
	mn_ac	0.64	24	0.0004
	fe_ac	0.67	24	0.0002
	ni_ac	0.65	24	0.0003
	cl	0.50	24	0.0098
	k	0.75	24	1.04E-05
	mg	0.80	24	9.83E-07
	ca	0.72	24	2.84E-05
	al_s	-0.61	22	0.0014
	fe_s	0.64	22	0.0007
	ag_s	-0.59	22	0.0024
Clique 4	temp	0.40	25	0.0394
	doc	0.52	21	0.0102
	doc_d13	0.48	21	0.0211
	tc_d13	0.48	23	0.0160
	continued			
	cu_ac	0.48	24	0.0136
	ag_ac	0.48	24	0.0133
	li	0.55	24	0.0035
	na	0.54	24	0.0048
Clique 5	cl	0.39	24	0.0464
	br	0.46	24	0.0177
	k	0.47	24	0.0165
	mg	0.45	24	0.0218
Clique 6	mn_ac	0.41	24	0.0357
	si	0.47	19	0.0305
Clique 7	temp	-0.45	25	0.0175
	do	0.73	25	1.85E-05
	spc	-0.44	25	0.0201
	ch4	0.96	17	4.87E-11
Clique 8	cd_ac	0.49	24	0.0116
	po4	0.43	24	0.0281
	cd_s	0.53	22	0.0080
Clique 9	**ph**	0.53	25	0.0047
	dic_d13	-0.53	21	0.0099
	doc_d13	-0.69	21	0.0003
	toc	0.53	23	0.0059
	tc	0.66	23	0.0003
	tn	0.83	23	2.86E-07
	tn_d15	-0.80	23	1.68E-06
	zn_ac	-0.50	24	0.0092
	f	0.74	24	0.0000
	no3	0.60	24	0.0012
	po4	-0.52	24	0.0064
	si	-0.71	19	0.0003
	cr_s	0.62	22	0.0012
Clique 10	**cr_ac**	0.57	24	0.0024
	cu_s	0.47	22	0.022
	ag_s	0.41	22	0.0445
	prot	0.6	18	0.0053
	cho	0.62	16	0.0064
	lip	0.49	18	0.0299
	feo	0.75	18	0.0001

Table S7. clique_spearman. Results of the Spearman rank correlation between the cumulative abundance of the ASVs in each clique and environmental variables. Only correlations with p<0.01 are reported.

Cliques	Factor	rho	adj. p
Clique 1	li	0.84	6.38E-08
	doc_d13	0.84	5.64E-07
	co2	0.86	2.19E-06
	po4	0.78	2.36E-06
	doc	0.81	2.68E-06
	zn_ac	0.69	1.04E-04
	na	0.65	2.95E-04
	so4	0.65	3.38E-04
	co2_he3	0.75	3.70E-04
	temp	0.62	6.09E-04
	k	0.62	7.98E-04
	h2s	-0.74	1.00E-03
	cu_ac	0.55	3.65E-03
	mg	0.53	5.70E-03
	dic	0.55	6.79E-03
Clique 2	k	-0.78	3.16E-06
	dic_d13	-0.79	5.97E-06
	ni_s	0.75	2.66E-05
	mn_ac	-0.72	3.70E-05
	zn_ac	-0.70	6.63E-05
	cr_s	0.72	6.79E-05
	cl	-0.67	1.94E-04
	ni_ac	-0.66	2.52E-04
	al_ac	0.66	2.76E-04
	dic	-0.69	3.05E-04
	spc	-0.62	5.92E-04
	fe_ac	-0.63	5.93E-04
	mg	-0.63	6.37E-04
	ph	0.61	6.83E-04
	li	-0.62	7.81E-04
	br	-0.61	1.02E-03
	ca	-0.61	1.03E-03
	temp	-0.58	1.58E-03
	co2	-0.66	2.30E-03
	doc_d13	-0.58	3.44E-03
	po4	-0.54	4.70E-03
	cd_ac	-0.52	6.70E-03
	so4	-0.51	8.13E-03
	cu_ac	-0.51	8.43E-03
	rc_ra	-0.55	9.72E-03
Clique 3	k	0.87	1.00E-08
	ni_s	-0.80	2.94E-06
	mg	0.78	3.14E-06
	ni_ac	0.74	1.83E-05
	spc	0.72	2.11E-05
	cr_s	-0.75	2.15E-05
	li	0.73	2.55E-05
	zn_ac	0.72	3.26E-05
	mn_ac	0.71	4.41E-05
	co2	0.63	4.13E-03
	rc_ra	0.59	4.51E-03
	no3	-0.52	6.64E-03
	doc	0.55	6.84E-03
	cu_ac	0.50	9.03E-03
	h2	-0.58	9.13E-03
	tc_d13	0.51	9.53E-03
	na	0.50	9.71E-03
Clique 4	li	0.81	4.34E-07
	doc	0.80	5.83E-06
	doc_d13	0.75	3.97E-05
	na	0.67	1.70E-04
	temp	0.65	2.63E-04
	co2	0.73	4.25E-04
	co2_he3	0.70	1.36E-03
	po4	0.58	2.06E-03
	h2	-0.66	2.21E-03
	so4	0.57	2.56E-03
	zn_ac	0.56	3.11E-03
	h2s	-0.67	4.17E-03
	cu_ac	0.52	6.59E-03
	k	0.50	9.15E-03
	spc	0.49	9.81E-03
Clique 5	li	0.68	1.29E-04
	temp	0.65	2.19E-04
	doc	0.70	2.26E-04
	h2	-0.72	5.15E-04
	doc_d13	0.67	5.19E-04
	k	0.62	8.06E-04
	h2s	-0.75	8.63E-04
	zn_ac	0.58	1.85E-03
	co2	0.66	1.95E-03
	spc	0.57	2.08E-03
	ni_s	-0.55	5.56E-03
	dic	0.56	5.60E-03
	na	0.53	5.64E-03
	cl	0.53	5.87E-03
Clique 6		none below p<0.01	
Clique 7	f	-0.63	5.30E-04
	cr_ac	0.58	2.08E-03
	so4	-0.56	2.64E-03
	spc	-0.54	3.71E-03
	al_s	0.55	5.80E-03
	cu_s	0.52	8.58E-03
Clique 8	co_ac	0.59	1.35E-03
	cl	-0.56	2.67E-03
	br	-0.56	2.81E-03
	cu_ac	-0.52	5.90E-03

cl	0.71	4.47E-05	Clique 9	dic	-0.83	8.32E-07
temp	0.70	5.62E-05		zn_ac	-0.76	6.59E-06
ca	0.70	7.05E-05		po4	-0.70	6.43E-05
fe_ac	0.69	9.82E-05		doc_d13	-0.70	1.79E-04
al_ac	-0.67	1.66E-04		mg	-0.64	4.30E-04
dic	0.70	1.77E-04		co2	-0.73	4.35E-04
dic_d13	0.70	2.03E-04		mn_ac	-0.64	4.72E-04
br	0.65	2.94E-04		li	-0.59	1.36E-03
doc_d13	0.67	5.29E-04		k	-0.59	1.50E-03
cu_s	-0.64	6.93E-04		dic_d13	-0.61	1.82E-03
so4	0.62	7.01E-04		doc	-0.60	2.71E-03
al_s	-0.61	1.63E-03		al_ac	0.55	3.67E-03
h2s	-0.71	2.08E-03		temp	-0.53	4.90E-03
cd_ac	0.57	2.19E-03		tn_d15	-0.53	6.24E-03
po4	0.56	2.92E-03		si	-0.58	6.29E-03
fe_s	0.56	4.05E-03		ph	0.50	8.61E-03
	continued		Clique 10		none below p<0.01	

Table S8. random_forests. Results of the Random Forests (RF) approach to the identification of the environmental explanatory variables for the distribution of each clique across the sampled hot springs. Only the top 15 environmental variables are reported in ranking order. *Thresh. var.* - number of variables that passed the Important Variable threshold; *interpr. var.* - number of variables identified as important in interpreting the clique distribution. Interpetation variables are marked in bold.

			Environmental variable importance ranking in Random Forests interpretation														
Cliques	**thresh. var.**	**interp. var.**	**1**	**2**	**3**	**4**	**5**	**6**	**7**	**8**	**9**	**10**	**11**	**12**	**13**	**14**	**15**
Clique 1	48	4	**doc**	**so4**	**li**	**ar**	co2	n2	co2_he3	zn_s	nh4	ah	doc_d13	co2_d13	po4	na	ch4
Clique 2	38	4	**ph**	**al_ac**	**n2**	**k**	ar	fe_ac	ni_ac	ca	ni_s	o2	h2	cr_s	cl	co2	na
Clique 3	40	5	**fe_s**	**ca**	**cu_s**	**ag_s**	**k**	ni_s	al_s	mg	ni_ac	fe_ac	mn_ac	cr_s	al_ac	zn_s	spc
Clique 4	19	1	**doc_d13**	li	doc	pah	hi_pah	tc_d13	ag_ac	ah	temp	co2_he3	mn_s	h2s	co2	cpe	co_ac
Clique 5	19	4	**br**	**cl**	**spc**	**h2**	temp	tn	zn_ac	dic	co2	tc_d13	dic_d13	cpe	co2_d13	h2s	li
Clique 6	5	1	**h2s**	h2	ch4	lip	n2										
Clique 7	27	1	**ch4**	**do**	**toc**	**tc**	so4	temp	na	spc	cu_ac	cho	li	lip	ph	co_ac	br
Clique 8	22	5	**br**	**ar**	**n2**	**cu_ac**	**co_ac**	cl	tn_d15	h2s	al_s	si	ah	cd_ac	cd_s	na	hi_pah
Clique 9	39	4	**dic**	**si**	**f**	**tn_d15**	po4	cpe	no3	tn	doc	doc_d13	mg	cr_s	ni_s	zn_ac	mn_ac
Clique 10	61	1	**cho**	feo	co2_d13	ag_ac	cha	o2	cr_ac	ag_s	lip	cu_s	dic	prot	alt	zn_ac	rc_ra

Table S9. consensus_environmental_variable. Table reporting the top environmental variables selected using the different techniques (scatterplot inspection, Spearman rank correlation, Pearson moment correlation, Random Forests) and the selected variable plotted in Figure 4 for each clique. For Spearman and RF only the top 15 variable were reported. In the Pearson column the bold variables have a p<0.01, while in the Rf column the bold variables are those selected by the model.

	Clique 1				Clique 2				Clique 3				Clique 4				Clique 5			
Var. Ranking	**R^2**	**Spearman**	**Pearson**	**RF**	**R^2**	**Spearman**	**Pearson**	**RF**	**R^2**	**Spearman**	**Pearson**	**RF**	**R^2**	**Spearman**	**Pearson**	**RF**	**R^2**	**Spearman**	**Pearson**	**RF**
1	temp	li	**zn_s**	**doc**	temp	k	**n2**	**ph**	temp	k	**mg**	**fe_s**	temp	li	**li**	**doc_d13**	temp	li	k	**br**
2	doc	doc_d13	**li**	**so4**	ph	dic_d13	**al_ac**	**al_ac**	spc	ni_s	**k**	**ca**	doc	doc	**na**	li	do	temp	br	**cl**
3	dco_d13	co2	**so4**	**li**	dic	ni_s	**ar**	**n2**	dic_d13	mg	**ca**	**cu_s**	na	doc_d13	doc	doc		doc	mg	**spc**
4	so4	po4	**nh4**	**ar**	dic_d13	mn_ac	**ph**	**k**	doc_d13	ni_ac	**fe_ac**	**ag_s**	cu_ac	na	ag_ac	pah		h2	cl	**h2**
5	po4	doc	**co2_he3**	co2	doc_d13	zn_ac	**ni_s**	ar	k	spc	**ni_ac**	**k**		temp	cu_ac	hi_pah		doc_d13		temp
6	li	zn_ac	**doc**	n2	al_ac	cr_s	**cr_s**	fe_ac	ca	cr_s	**mn_ac**	ni_s		co2	tc_d13	tc_d13		k		tn
7	na	na	**na**	co2_he3	ni_s	cl	**h2**	ni_ac		li	**fe_s**	al_s		co2_he3	doc_d13	ag_ac		h2s		zn_ac
8	k	so4	**po4**	zn_s		ni_ac	**o2**	ca		zn_ac	**al_s**	mg		po4	temp	ah		zn_ac		dic
9	ca	co2_he3	**doc_d13**	nh4		al_ac	**co2**	ni_s		mn_ac	**ag_s**	ni_ac		h2		temp		co2		co2
10	zn_ac	temp	**ah**	ah		dic	**dic_d13**	o2		cl	**spc**	fe_ac		so4		co2_he3		spc		tc_d13
11		k		doc_d13		spc	**temp**	h2		temp	**cl**	mn_ac		zn_ac		mn_s		ni_s		dic_d13
12		h2s		co2_d13		fe_ac	**cl**	cr_s		ca		cr_s		h2s		h2s		dic		cpe
13		cu_ac		po4		mg		cl		fe_ac		al_ac		cu_ac		co2		na		co2_d13
14		mg		na		ph		co2		al_ac		zn_s		k		cpe		cl		h2s
15		dic		ch4		li		na		dic		spc		spc		co_ac				li
Selected Var.	**doc**				**ph**				**fe_ac**				**doc**				**do**			

	Clique 6				Clique 7				Clique 8				Clique 9				Clique 10			
Var. Ranking	**R^2**	**Spearman**	**Pearson**	**RF**	**R^2**	**Spearman**	**Pearson**	**RF**	**R^2**	**Spearman**	**Pearson**	**RF**	**R^2**	**Spearman**	**Pearson**	**RF**	**R^2**	**Spearman**	**Pearson**	**RF**
1	none	none below p<0.01	si	**h2s**	cu_s	f	**ch4**	**ch4**	cr_ac	co_ac	**cd_s**	**br**	temp	dic	**tn**	**dic**	none	none below p<0.01	**feo**	**cho**
2			mn_ac	h2	cr_ac	cr_ac	**do**	**do**	co_ac	cl	cd_ac	**ar**	dic	zn_ac	**tn_d15**	**si**			**cr_ac**	feo
3				ch4		so4	temp	**toc**	cl	br	po4	**n2**	dic_d13	po4	**f**	**f**			**prot**	co2_d13
4				lip		spc	spc	**tc**	cu_s	cu_ac		**cu_ac**	doc_d13	doc_d13	**doc_d13**	**tn_d15**			**cho**	ag_ac
5				n2		al_s		so4	ag_s			**co_ac**	al_ac	mg	**si**	po4			cu_s	cha
6						cu_s		temp				cl	po4	co2	**tc**	cpe			lip	o2
7								na				tn_d15	no3	mn_ac	**cr_s**	no3			ag_s	cr_ac
8								spc				h2s	k	li	**no3**	tn				ag_s
9								cu_ac				al_s	mg	k	**ph**	doc				lip
10								cho				si	ni_s	dic_d13	**toc**	doc_d13				cu_s
11								li				ah	si	doc	**po4**	mg				dic
12								lip				cd_ac		al_ac	**zn_ac**	cr_s				prot
13								ph				cd_s		temp	**dic_d13**	ni_s				alt
14								co_ac				na		tn_d15		zn_ac				zn_ac
15								br				hi_pah		si		mn_ac				rc_ra
Selected Var.	**none**				**ch4**				**cu_s**				**dic**				**none**			

Supplementary Figures

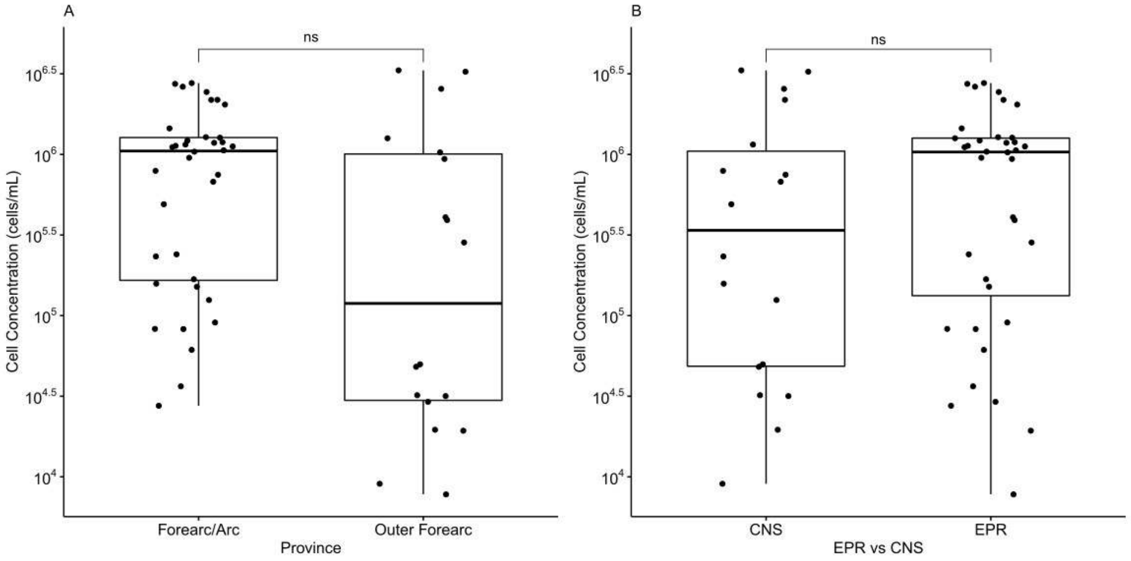

Figure S1. Cell counts on fluids, measured by flow cytometry.

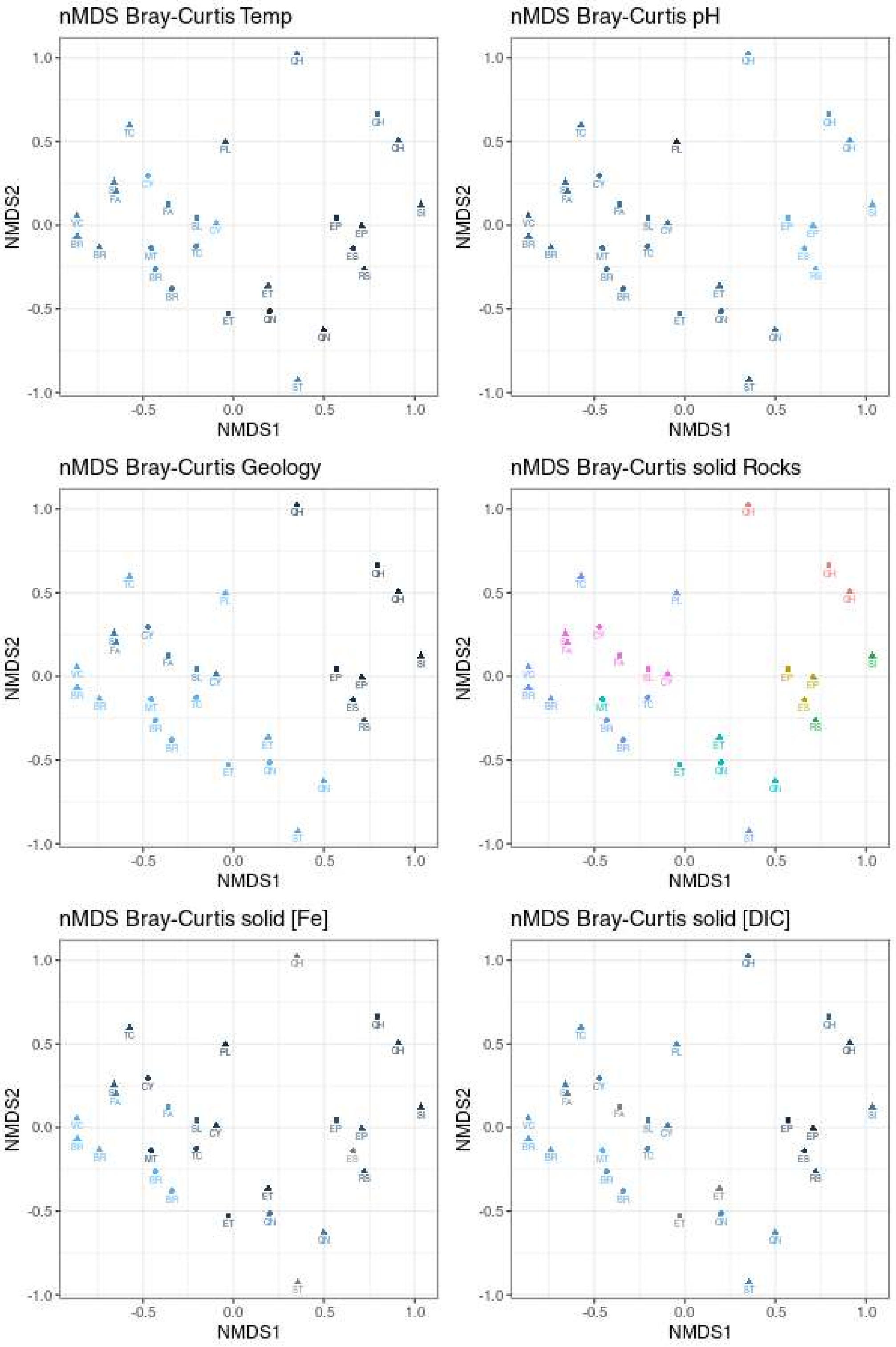

Figure S2. Supplementary figure ord_comparison. NMDS plot based on Jaccard similarity index colored by different environmental variables. Temperature, pH, geol_prov, rocks, $[Fe]_s$ and [DIC].

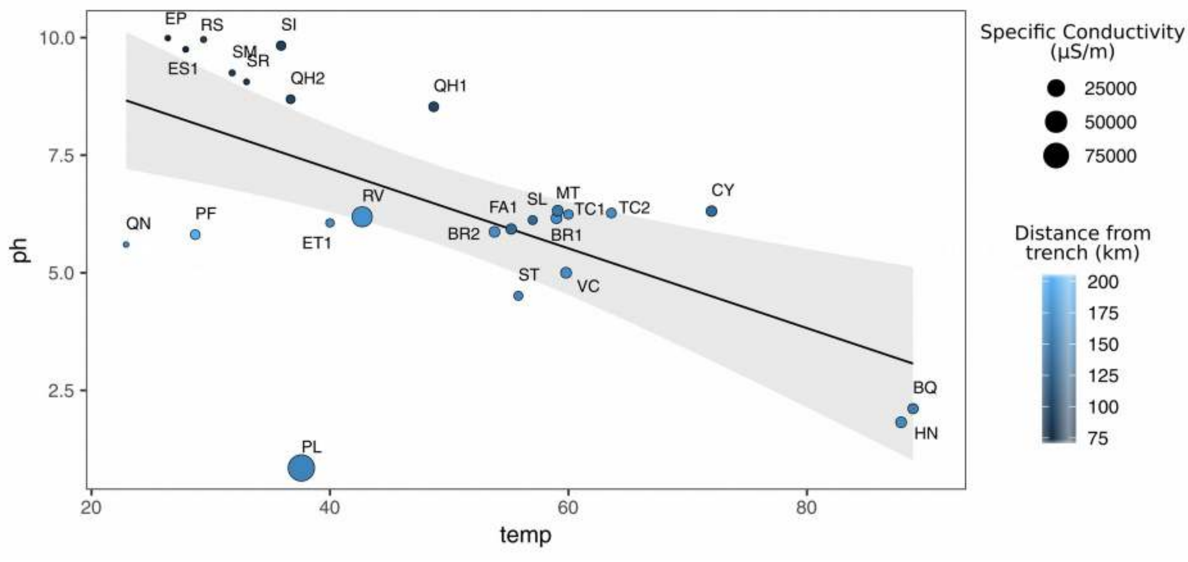

Figure S3. Supplementary temperature_ph. Plot showing the relationship between temperature, pH, specific conductivity and distance from trench for the sampled hot springs. The correlation between temperature and pH measurements carried out in the field is -0.602. Poas Lake (PL) sample fall significantly below the trend line. The measured temperature of the lake waters was significantly influenced by the low activity of the caldera during the sampling days. The activity increased in the following weeks, completely evaporating the lake water. Based on the combined geochemical and microbiological data we expected the lake temperature to be >80°C at the time of sampling, and suggest that the measured temperature on the day of sampling is an outlier, sowing momentary temperature below the expected range.

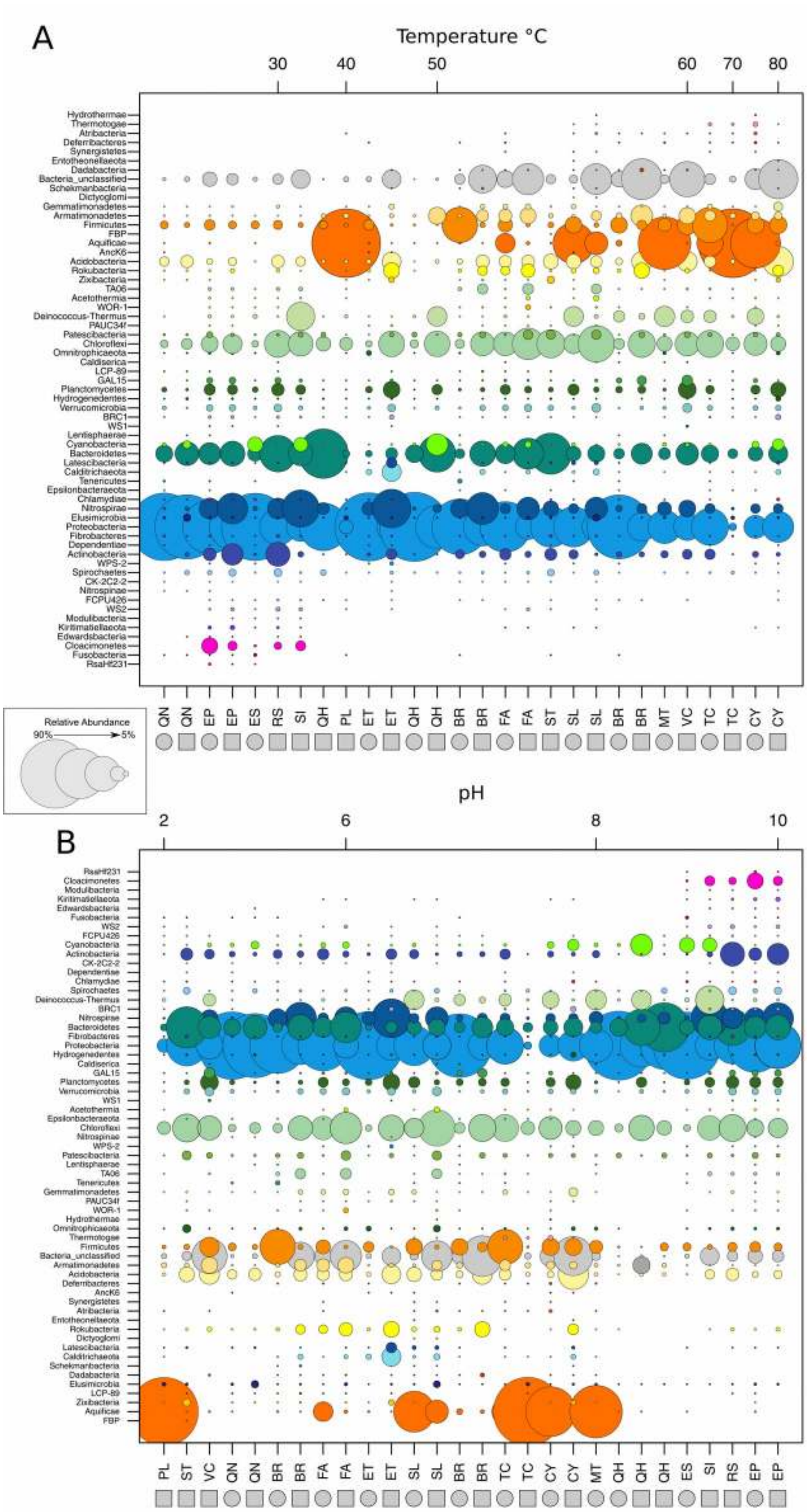

Figure S4. Plot of the relative abundance of the identified bacterial phyla in the sample stations ordered by site temperature (A) and pH (B) respectively. The size of the circle is proportional to the relative abundance of the taxa, squares are sediments and circles are fluids, and vertical ordering is by strength of correlation with temperature (A) and pH (B).

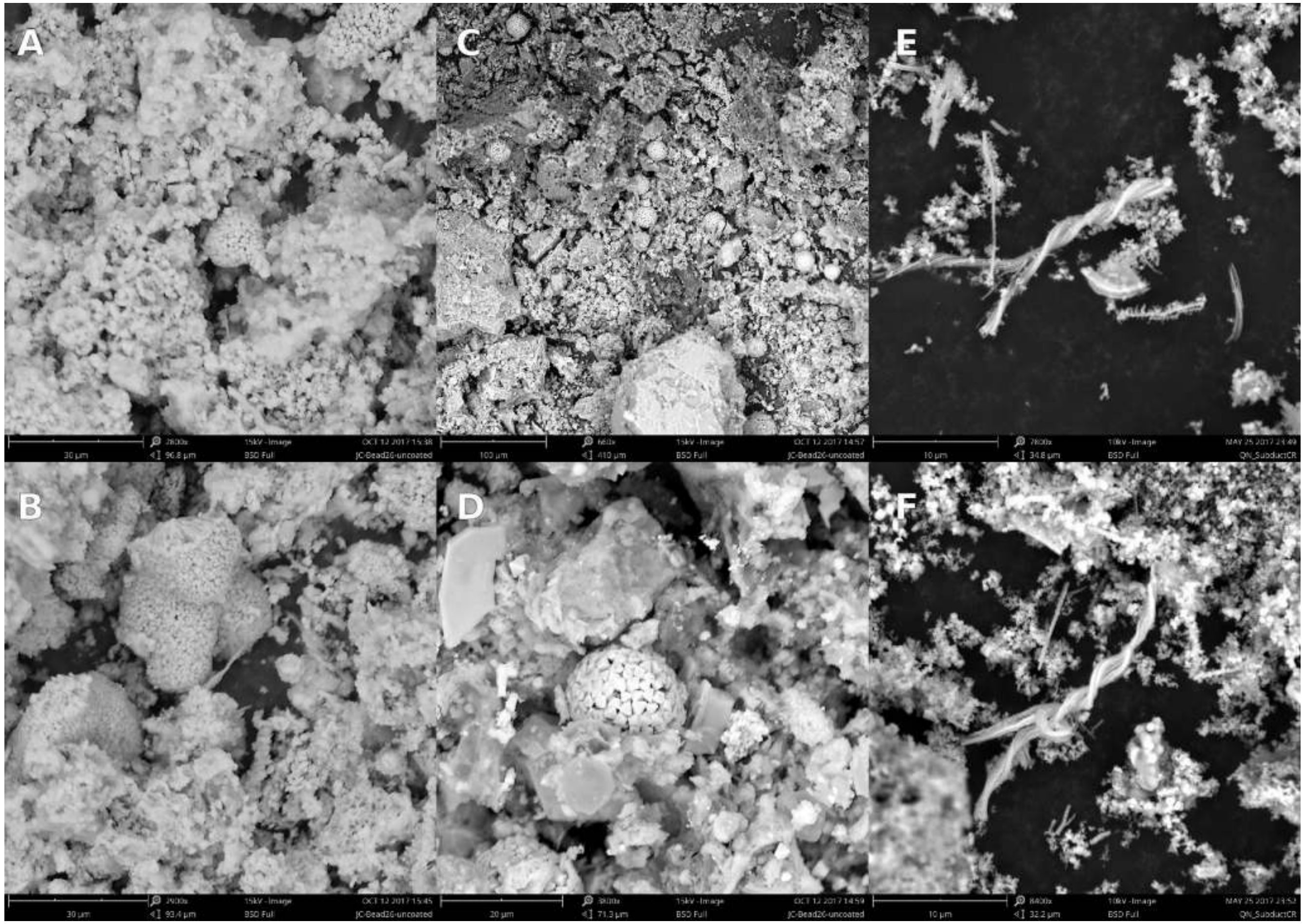

Fig. S5. Scanning electron microscope micrographs representative of the mineral morphologies identified in the sediments of selected hot springs. A, B – Blue River (BR) site; C, D – Santa Lucia (SL) site, pyrite framboids are clearly visible in this samples suggesting iron sulfide precipitations; E, F – Quebrada Naranja (QN) site, iron hydroxide twisted stalks are clearly visible in the sample suggesting active microbial iron oxidation.

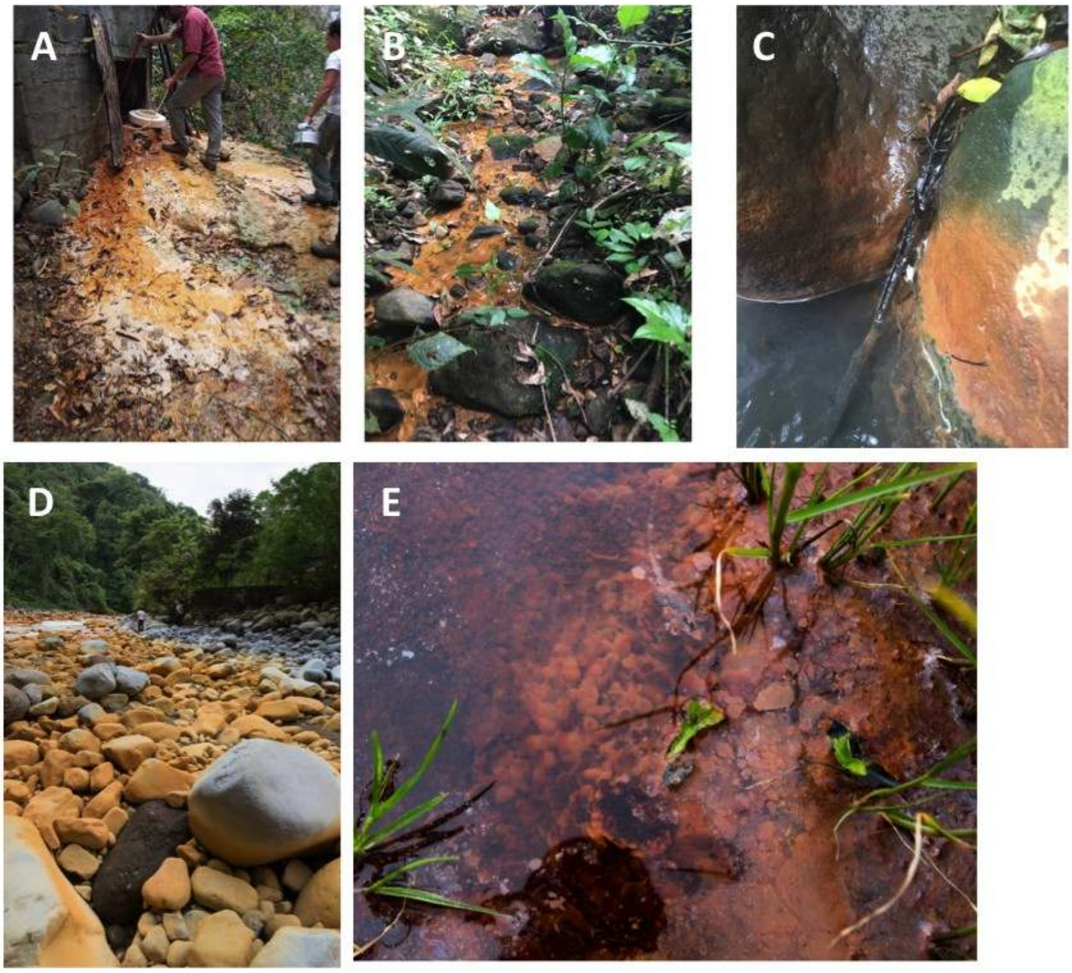

Fig. S6. Photographs of visible iron deposits at A) Rio Cayuco, CY, B), Quebrada Naranja, QN, C) El Tucano, TC, D) Recreo Verde, RV, and E) Santa Theresa, ST. These sites are all in the central forearc/arc. No sites in the northern Guanacaste calderas, or the outer forearc had iron deposits like this.

Fig. S7. Photographs showing lack of largescale iron deposits in the northern forearc/arc. Shown are A-San Lucia (SL), B-Volcancito (VC), C-Bourinquen (BQ), D-Finca Ande (FA), E-Mouse Trap (MT), F-Eco Termales (ET), and G-Las Hornillas (HN).

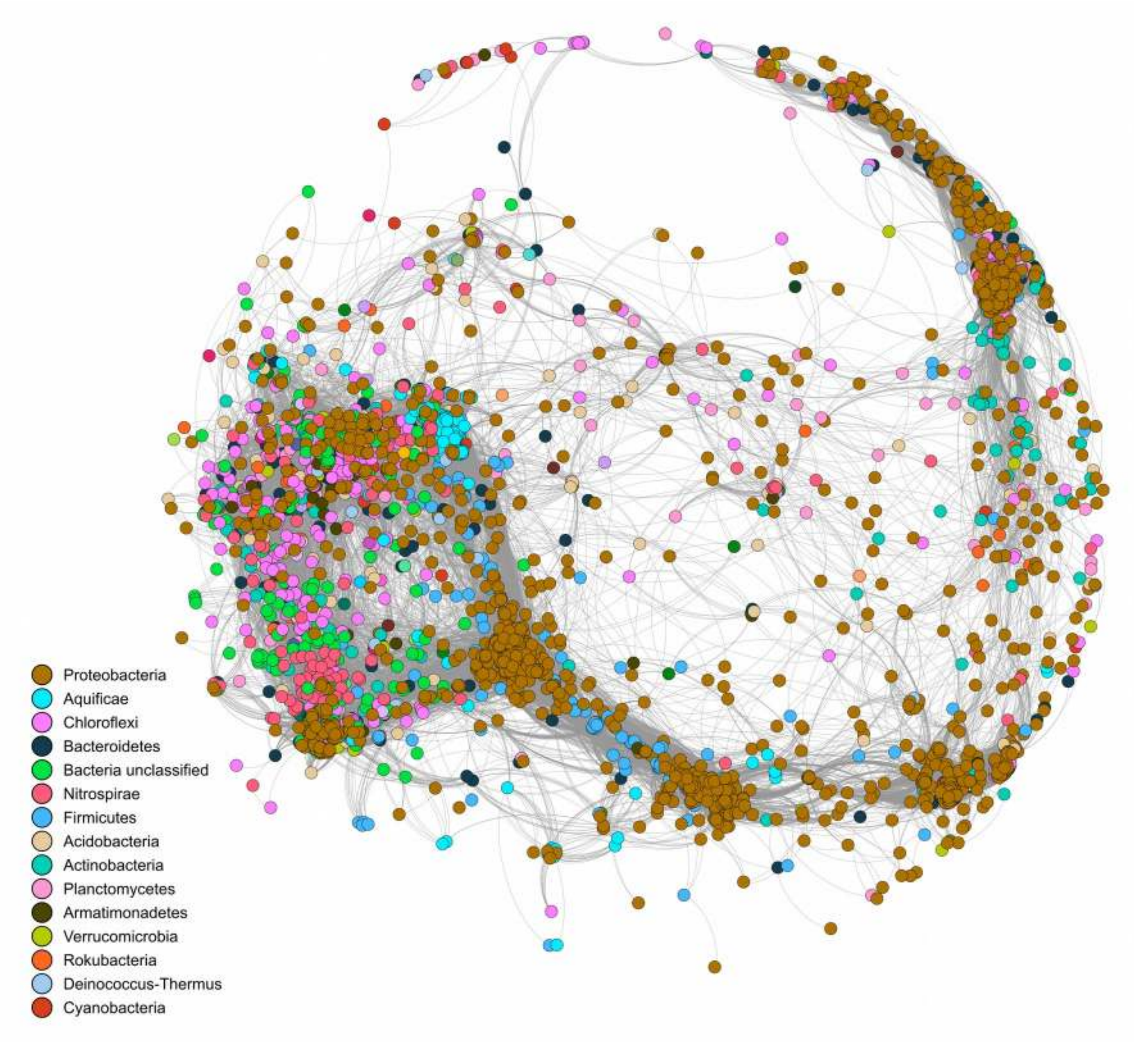

Fig. S8. Co-occurrence network of the dominant ASVs in the fluids and sediments presented in Figure 4 colored by Phyla. ASVs are represented by vertex, edges represent pairwise Spearman correlations above 0.65.

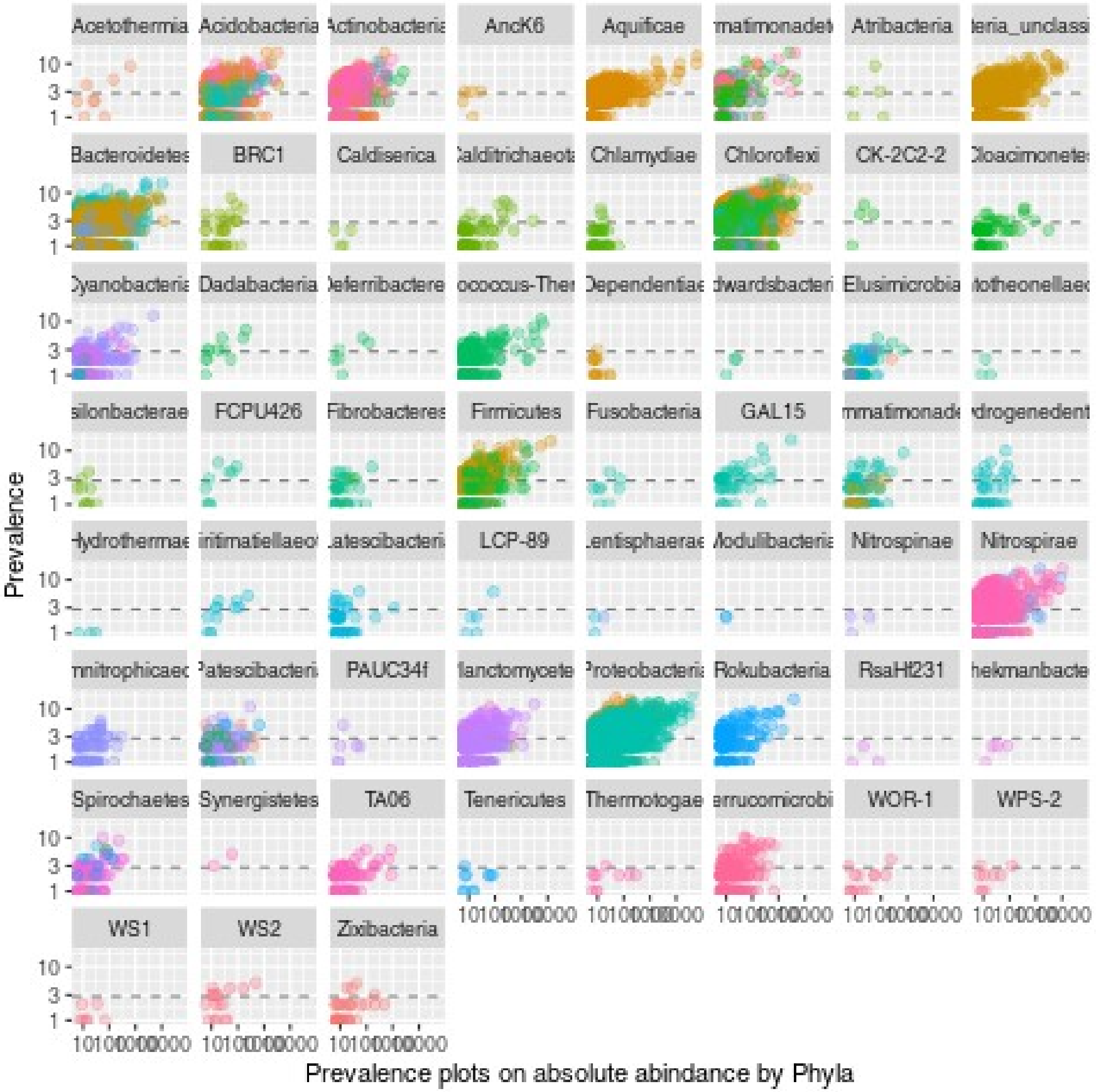

Fig. S9. Prevalence analysis of the 16S rRNA bacterial community across the investigated samples. Amplicon Sequencing Variants (ASV) with abundance of normalized reads below 5 were removed.